Hafiz Asad Ali Awan

Discrete-Time Current Control of Synchronous Motor Drives

School of Electrical Engineering

Thesis submitted for examination for the degree of Master of Science in Technology.

Espoo 23.02.2015

Thesis supervisor:

Prof. Marko Hinkkanen

Thesis advisor:

Zengcai Qu, M.Sc. (Tech.)

Aalto University
School of Electrical
Engineering

AALTO UNIVERSITY
SCHOOL OF ELECTRICAL ENGINEERING

ABSTRACT OF THE
MASTER'S THESIS

Author: Hafiz Asad Ali Awan

Title: Discrete-Time Current Control of Synchronous Motor Drives

Date: 23.02.2015 Language: English Number of pages:9+60

Department of Electrical Engineering and Automation

Professorship: Electric Drives Code: S-81

Supervisor: Prof. Marko Hinkkanen

Advisor: Zengcai Qu, M.Sc. (Tech.)

The aim of this thesis is to analyze discrete-time models and current control of synchronous motors with a magnetically anisotropic rotor structure, such as interior permanent-magnet synchronous motors (IPMSMs) and synchronous reluctance motors (SyRMs). Current regulators in most modern electrical drives are implemented in digital processors. Discretization of continuous-time controllers using the Euler and Tustin approximations, also known as the emulation-based design, is the most common approach. This design gives satisfactory results when the ratio between the sampling and fundamental frequencies remains high. The performance of the emulation-based design deteriorates as the frequency ratio becomes small. For this reason, the controller based on the exact discrete-time model of the machine is preferred. If the exact expressions are computationally too demanding, approximate expressions (series expansions) could be used instead. A hold equivalent discrete-time model with the effects of the zero-order hold (ZOH) and a sampler is studied in both the stator and rotor coordinates. A two-degrees-of-freedom (2DOF) state-space controller is used with the gains based on the exact discrete-time model of the motor. The results are compared with the emulation- and series expansions (of the exact discrete-time model) based controllers. The robustness of these methods against parameter errors is analyzed and the current controllers are also investigated by performing simulations and experiments on a 6.7-kW SyRM drive.

Keywords: Current control, discrete, interior permanent-magnet synchronous motors (IPMSMs), state-space controller, synchronous reluctance motors (SyRMs), two-degrees-of-freedom (2DOF)

Preface

The research work reported in this thesis has been done at Aalto University, Department of Electrical Engineering and Automation. The work has been financially supported by ABB Oy, as a part of an ongoing research project on electric drives.

First of all, thanks to Almighty Allah, the Most Gracious, the Most Merciful, who guides me on every step I take. I would like to express my deepest gratitude to my supervisor Prof. Marko Hinkkanen for giving me this wonderful opportunity to work in this research project. I would like to thank him for his guidance, valuable suggestions and useful corrections in scientific writing. My advisor, Mr. Zengcai Qu helped me in understanding the experimental setup and doing simulations. This thesis is part of an ongoing research project and the previous work done by Prof. Marko Hinkkanen and Dr. Toni Tuovinen was helpful in understanding the subject.

I would like to thank Dr. Antti Piippo, Dr. Toni Tuovinen and others from ABB Oy, Finland for their constructive comments and suggestions throughout the thesis. I would like to thank all of my colleagues at electric drives research group for their advice and suggestions. I would also like to thank my friends Amjad Hussain and Farhan Mahmood for their support and guidance.

Finally, I would like to thank my whole family, especially my parents for their endless support throughout my life.

Espoo, 23.02.2015

Hafiz Asad Ali Awan

Contents

Symbols and Abbreviations

Symbols

Complex-valued variables are underlined and boldface letters represent matrices and vectors. Reference values are marked by the subscript ref.

$\underline{a}_{0\mathrm{c}}$, $\underline{a}_{0\mathrm{c}}$, $\underline{b}_{1\mathrm{c}}$, $\underline{b}_{1\mathrm{c}}$	Coefficients of the reference-following transfer function
$\underline{a}_{0\mathrm{c}\star}$, $\underline{a}_{1\mathrm{c}\star}$, $\underline{b}_{1\mathrm{c}\star}$, $\underline{b}_{1\mathrm{c}\star}$	Intended coefficients of the reference-following transfer function for an SPMSM
$\boldsymbol{A}_0$, $\boldsymbol{A}_1$, $\boldsymbol{A}_2$, $\boldsymbol{B}_0$, $\boldsymbol{B}_1$	Coefficient matrices for a discrete-time reference-following transfer function
$\underline{a}$	Discrete-time current coefficient
$\boldsymbol{A}$	Discrete-time system matrix with current as a state variable
$\underline{a}_\mathrm{c}$	Continuous-time current coefficient
$\boldsymbol{A}_\mathrm{c}$	Continuous-time system matrix with flux as a state variable
$\boldsymbol{A}_\mathrm{d}$	Discrete-time system matrix with flux as a state variable
$\underline{b}$	Discrete-time voltage coefficient with current as a state variable
$\boldsymbol{B}$	Discrete-time voltage input matrix with current as a state variable
$\underline{b}_\mathrm{c}$	Continuous-time voltage coefficient
$\boldsymbol{b}_\mathrm{c}$	Continuous-time permanent-magnet flux input matrix
$\boldsymbol{B}_\mathrm{c}$	Continuous-time voltage input matrix
$\boldsymbol{b}_\mathrm{d}$	Discrete-time permanent-magnet flux input matrix
$\boldsymbol{B}_\mathrm{d}$	Discrete-time voltage input matrix
$\underline{b}'$	Discrete-time voltage coefficient with the ZOH in rotor coordinates
$\underline{b}_\psi$	Discrete-time permanent-magnet flux coefficient
$\underline{b}_{\psi\mathrm{c}}$	Continuous-time permanent-magnet flux coefficient
$\boldsymbol{C}$	Inverse inductance matrix
$\boldsymbol{d}$	Discrete-time permanent-magnet flux input matrix with current as a state variable

dq	Synchronous or rotating coordinates
e, $\boldsymbol{e}$	Error signal input to the current controller
$\boldsymbol{F}$	Taylor series expansion
f_s	Sampling frequency
f_sw	Switching frequency
$\boldsymbol{I}$	2×2 identity matrix
i_d	d-axis component of the stator current
i_q	q-axis component of the stator current
$\underline{i}_\mathrm{s}$	Stator current complex space vector
$\boldsymbol{i}_\mathrm{s}$	Stator current real space vector
$\boldsymbol{i}_\mathrm{s,ripple}$	Average ripple current
$\boldsymbol{i}_\mathrm{s,total}$	Total stator current (sum of the sampled and ripple current)
j	Imaginary unit
$\boldsymbol{J}$	Orthogonal rotation matrix
J	Total moment of inertia for a system
k	Sampling instant
$\underline{k}_1$	Discrete-time state feedback gain
$\boldsymbol{K}_1$	Discrete-time state feedback gain matrix
$\underline{k}_2$	Discrete-time voltage state feedback gain
$\boldsymbol{K}_2$	Discrete-time voltage state feedback gain matrix
$\underline{k}_\mathrm{1c}$	Continuous-time state feedback gain
$\underline{k}_\mathrm{2c}$	Continuous-time voltage state feedback gain
$\underline{k}_\mathrm{i}$	Discrete-time integral gain
$\underline{k}_\mathrm{ic}$	Continuous-time integral gain
$\boldsymbol{K}_\mathrm{i}$	Discrete-time integral gain matrix
$\underline{k}_\mathrm{t}$	Discrete-time feedforward gain
$\underline{k}_\mathrm{tc}$	Continuous-time feedforward gain
$\boldsymbol{K}_\mathrm{t}$	Discrete-time feedforward gain matrix
L_s	Stator inductance
$\boldsymbol{L}_\mathrm{s}$	Inductance matrix

L_d	Direct-axis inductance
L_q	Quadrature-axis inductance
$\mathbf{0}$	2×1 null vector
$\boldsymbol{O}$	2×2 null matrix
p_1, $p_{1\star}$	Real pole and intended real pole
R_s	Stator resistance
t	Time variable
T_e	Electromagnetic torque
T_L	Load torque
T_s	Sampling period
u_d	d-axis component of the stator voltage
$\underline{u}_\mathrm{i}$	Back-emf voltage
u_q	q-axis component of the stator voltage
$\underline{u}_\mathrm{s}$	Stator voltage complex space vector
$\boldsymbol{u}_\mathrm{s}$	Stator voltage real space vector
$\underline{u}'_\mathrm{s,ref}$	Reference voltage-output of the current controller
x_i, $\boldsymbol{x}_\mathrm{i}$	Integral state of the current controller
α	Current controller bandwidth
$\alpha\beta$	Stationary or stator coordinates
ϑ_m	Electrical angle
μ_r	Relative permeability
$\boldsymbol{\Phi}$	Overall system matrix
ψ_d	d-axis component of the stator flux
ψ_pm	Permanent-magnet flux
$\boldsymbol{\psi}_\mathrm{pm}$	Permanent-magnet flux vector
ψ_q	q-axis component of the stator flux
$\underline{\psi}_\mathrm{s}$	Stator flux complex space vector
$\boldsymbol{\psi}_\mathrm{s}$	Stator flux real space vector
ω_m	Electrical angular speed

Abbreviations

2DOF	Two-degrees-of-freedom
AC	Alternating current
DTC	Direct torque control
PM	Permanent magnet
IMC	Internal model control
IM	Induction motor
IPMSM	Interior permanent-magnet synchronous motor
PI	Proportional integral
PMSM	Permanent-magnet synchronous motor
PWM	Pulse-width modulation
SPMSM	Surface permanent-magnet synchronous motor
SyRM	Synchronous reluctance motor
ZOH	Zero-order-hold

Chapter 1

Introduction

1.1 Background

Electrical machines are used for electromechanical energy conversion. Nearly all of the world's electrical power is being produced by synchronous generators, whereas induction motors (IMs) are pre-dominantly used in large industrial to small household appliances for converting energy from electrical to mechanical [1]. Three-phase motors are employed mostly in the industry, whereas single-phase motors are abundantly used for household applications [1]. This trend of converting electrical energy to mechanical energy using IMs is being followed for over a century.

IMs are the common choice due to their low cost, simple realizability, robustness and the self-starting capability when connected directly to AC mains [2]. However, recent changes in European energy laws and Europe's 2020 goal to boost the energy efficiency up to 20% have increased the interest in going for more energy-efficient solutions. Energy efficiency is being considered the main driving factor now. Recent developments in the design of synchronous motors, power electronic circuits and permanent-magnet materials have made it possible to replace IMs with more efficient synchronous motors. Synchronous motors provide increased efficiency, a high torque-ampere ratio, small inertia and high power density compared with the IMs of the same rating [2]. The increase in efficiency is due to the absence of the rotor winding making the resistive losses small in the stator and almost negligible in the rotor. The increase in the magnetic and thermal capabilities of permanent-magnets (PMs) due to the increased usage of high-coercive PM-materials have made PM-synchronous machines more efficient, robust and compact [3]. High-coercive PM-materials are costly, but it is a compromise between the performance and cost.

Frequency converters are an essential part of an industrial control system when providing high performance, better energy efficiency and robust control for AC ma-

chines. Typically, an electric drive consists of an AC motor and a frequency converter between the mains and the motor. A frequency converter is usually a combination of a rectifier, dc-link (with capacitor) and a pulse-width modulated (PWM) inverter. Electric motors are significant consumers of electricity, nearly half of the global electricity is being consumed by the electric motors [4]. Therefore, there is a need to study and develop more effective control methods which are robust and of high performance.

Permanent-magnet synchronous motors (PMSMs) and synchronous reluctance motors (SyRMs) are increasingly applied in hybrid/electric vehicles (automotive industry), heavy-duty working machines and industrial applications. Despite the high cost of PMs, PMSMs are still considered as a better choice than IMs for automotive industry due to their increased efficiency, small size and robustness. Heavy-duty working electric machines may run at very high speeds and excitation frequencies (fundamental) can be as high as 1 kHz [5]. Controllers designed in continuous time (emulation-based design) are not suitable for providing good dynamic performance at high excitation frequencies. In the emulation-based design, the continuous-time controller is discretized for the digital implementation using the Euler or Tustin approximations [6–10]. In order to overcome the problem of poor performance at high excitation frequencies, different approaches can be used, one of them is the design of direct discrete-time controllers. Direct discrete-time controllers are preferred over continuous-time controllers because they provide better performance at low sampling to excitation frequency ratios (lower or nearly equal to 10) [5, 11–14]. It should be noted that the sampling frequency (f_{s}) is usually equal to or twice the switching frequency (f_{sw}).

Broadly speaking, two types of control methods are available for the control of AC motors, scalar and vector control. Scalar control is considered to be the simplest way of controlling AC motors, just by adjusting the magnitude of the stator voltage proportionally to the supply frequency [15, 16]. Due to this relationship between the voltage and frequency, this type of control is often called as the constant volts-per-hertz control. Scalar control is often used for fans or pumps where there is no need for high dynamic performance and accuracy [17]. It should be noted that the scalar-control methods cannot be used for controlling the electromagnetic torque of a motor. Vector-control methods are more advanced methods, they are used in drives where high dynamic performance and precision are needed. PMSMs and SyRMs are typically controlled using vector-control methods.

The increasing use of PMSMs and SyRMs has raised the interest in developing high-performance control structures. In order to control the stator current of synchronous motor drives, different control schemes have been developed among which the flux orientation control methods and the direct torque control (DTC) can be classified as vector control methods [15]. The stator current of synchronous motor drives is typically controlled in rotor coordinates [6–14, 18]. Vector control in rotor coordinates is a natural selection since the controllable quantities are transformed

from three-phase AC to two-component DC quantities. Furthermore, all the other parts of the control system are typically operated in rotor coordinates. Apart from the ease of control and better performance, the synchronous frame control is inherently prone to cross-coupling between the d- and q-axes. Transformation from the stationary reference frame (stator coordinates) to rotating reference frame (rotor coordinates) introduces speed dependent cross-coupling terms in the system [19]. These terms need to be decoupled in order to achieve high performance and robust control.

Different control algorithms and schemes have been proposed in the literature to cope with the problems of cross-coupling. The model-based control design of the synchronous frame proportional-integral (PI) controller with feedforward decoupling terms is used as one of the current regulation schemes [7, 18]. PI controllers are well understood and being used in industry for a long time, but they are not suitable for machines like interior permanent-magnet synchronous motors (IPMSMs) and SyRMs running at high speeds. The dynamic performance of the current regulator reduces significantly at low switching to excitation frequency ratios (less than 10) [18, 20]. Cross-coupling between the d- and q-axis quantities increases with the increase in the rotor speed. Furthermore, the controllers are designed in continuous time and then implemented digitally using the Euler and Tustin approximations [21]. Advancements in digital signal processors have increased the usage of discrete-time design methods over continuous-time. Furthermore, the continuous-time design limits the closed-loop bandwidth of the controller to below one tenth of the sampling frequency [5, 7].

1.2 Objective and Outline of the Thesis

The objective of this thesis is to implement and analyze the discrete-time models and current control for synchronous motors with a magnetically anisotropic rotor structure, such as IPMSMs and SyRMs. The exact discrete-time models and current control methods for an IPMSM and SyRM have been recently developed in an ongoing research project, cf. [5]. A two-degrees-of-freedom (2DOF) state-space controller is used to make a comparative study of the control based on different models of synchronous motors. A 2DOF state-space controller-design based on the exact discrete-time model of the synchronous motor is compared with the controller-design based on the approximate motor models (e.g., the series expansions of the exact discrete-time model). The emulation-based design (controller) will also be compared with the direct discrete-time design.

The thesis concentrates on the field oriented current control of a synchronous motor. A mechanical position sensor is used to measure the rotor position (angle). Furthermore, the current control is studied at a constant rotor speed ω_{m}. The selected models and controllers are simulated in Matlab/Simulink environment and the robustness of these methods against parameter errors is analyzed. Furthermore,

the performance of the controllers is also investigated by experiments on a 6.7-kW SyRM drive.

The thesis consists of five chapters. Chapter 2 introduces the continuous-time and discrete-time models of synchronous motors. Chapter 3 gives a detailed explanation about the current controller structure and its gain calculations. Gains of the current controller are calculated based on the exact and approximate discrete-time models of IPMSMs and SyRMs. The continuous-time controller and its discretization using numerical approximations are also presented. Stability analysis, simulations and experimental results are presented in Chapter 4. At the end, conclusions are drawn based on the results.

Chapter 2

Modelling of Synchronous Machines

Synchronous motors in terms of their rotor construction (magnetically) are broadly divided into two main types, i.e., salient and non-salient pole motors. The salient pole motors can be further divided into motors with the PMs buried inside their rotors (IPMSMs) and the rotors without permanent-magnets (SyRMs). PMs are used in the rotor instead of a separate field winding to reduce the rotor resistive losses and in turn increase the efficiency. Non-salient PMSMs are also called surface permanent-magnet synchronous motors (SPMSMs). It is clear from the name that the PMs are mounted on the surface of the rotor for SPMSMs. Salient-pole PMSMs or IPMSMs have PMs buried inside their rotor, thus changing the effective air-gap and inductance in the direction of the magnetic axis (d-axis). The effective air-gap in the d-axis direction is larger than in the q-axis direction, as the relative permeability of PMs is nearly equal to that of air, $\mu_{\mathrm{r}} = 1.05$. Therefore, it can be inferred that the inductance in the salient pole machine is dependent on the rotor position. In this chapter, the continuous-time and discrete-time models of these machines are developed and discussed.

2.1 Continuous-Time Model of an SPMSM

The construction of an SPMSM is simple, having a round rotor with PMs mounted on the surface of the rotor, making the inductance constant all over the air-gap. Furthermore, the inductance is not dependent on the rotor position because the relative permeability of PMs is comparable to air ($\mu_{\mathrm{r}} = 1.05$) which makes a uniform air-gap between the stator and rotor. The stator or armature of PMSMs is typically similar in construction to that of an induction motor [21]. The rotor has PMs which produce the essential flux in the air-gap.

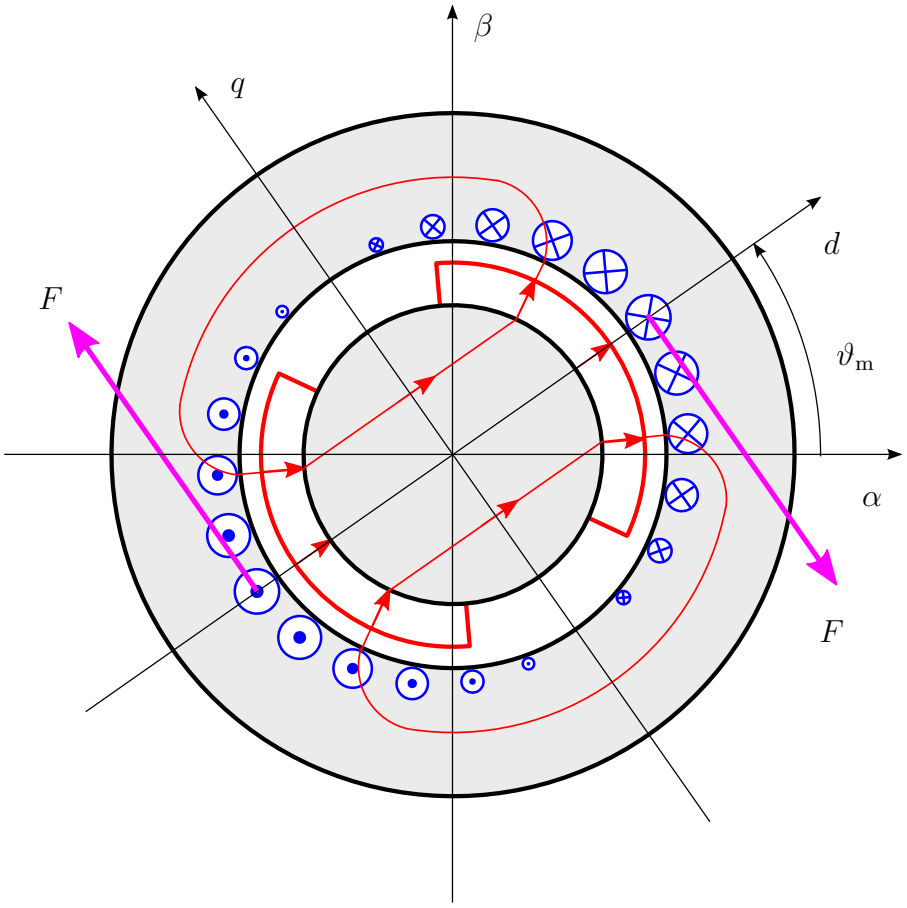

Figure 2.1: Conceptual diagram of a three-phase SPMSM [22].

Figure 2.1 shows the conceptual diagram of a 3-phase SPMSM, where the $\alpha\beta$ represent the stationary coordinates and dq shows the rotating or synchronous coordinates. The d-axis is oriented in the direction of the PM flux and the q-axis is orthogonal to the d-axis. The electrical angular speed of the rotor is denoted by ω_m and ϑ_m is the rotor angle given as

$$\vartheta_\mathrm{m}(t) = \int \omega_\mathrm{m} \mathrm{d}t \tag{2.1}$$

The equivalent circuit diagram of an SPMSM (in stator coordinates) is shown in Figure 2.2. The voltage equation is given as

$$\underline{u}_\mathrm{s}^\mathrm{s}(t) - R_\mathrm{s}\underline{i}_\mathrm{s}^\mathrm{s}(t) - \frac{\mathrm{d}\underline{\psi}_\mathrm{s}^\mathrm{s}(t)}{\mathrm{d}t} = 0 \tag{2.2}$$

where R_s is the stator resistance, $\underline{u}_\mathrm{s}^\mathrm{s}$ is the stator voltage vector, $\underline{i}_\mathrm{s}^\mathrm{s}$ is the stator current vector and $\underline{\psi}_\mathrm{s}^\mathrm{s}$ is the stator flux vector in stator coordinates. The time dependence of the vectors is given by t. The stator flux vector is given by

$$\underline{\psi}_\mathrm{s}^\mathrm{s}(t) = L_\mathrm{s}\underline{i}_\mathrm{s}^\mathrm{s}(t) + \underline{\psi}_\mathrm{pm}^\mathrm{s}(t) \tag{2.3}$$

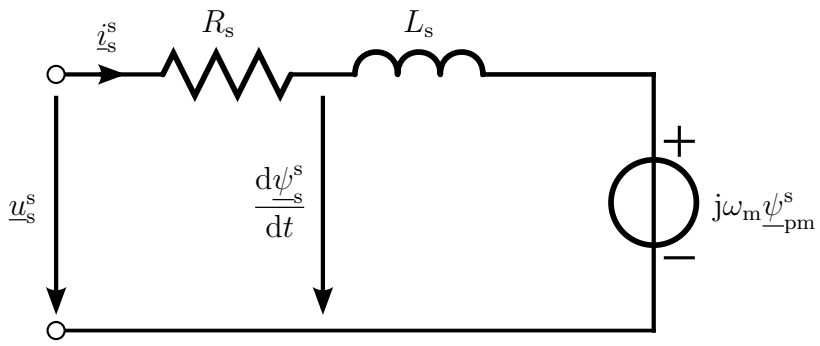

Figure 2.2: SPMSM equivalent circuit in stator coordinates.

where L_s is the stator inductance and $\underline{\psi}_\mathrm{pm}^\mathrm{s}(t)$ is the time-varying PM flux vector in stator coordinates.

From Figure 2.1, the PM flux $\underline{\psi}_\mathrm{pm}^\mathrm{s}$ defines the d-axis of the rotor which is displaced by an angle ϑ_m relative to the α-axis. In order to transform (2.2) and (2.3) to rotor coordinates with the PM flux rotating at a synchronous speed ω_m, following relations will be used

$$\underline{\psi}_\mathrm{pm}^\mathrm{s}(t) = \mathrm{e}^{\mathrm{j}\vartheta_\mathrm{m}(t)}\psi_\mathrm{pm} \tag{2.4a}$$

$$\underline{u}_\mathrm{s}^\mathrm{s}(t) = \mathrm{e}^{\mathrm{j}\vartheta_\mathrm{m}(t)}\underline{u}_\mathrm{s}(t) \tag{2.4b}$$

$$\underline{i}_\mathrm{s}^\mathrm{s}(t) = \mathrm{e}^{\mathrm{j}\vartheta_\mathrm{m}(t)}\underline{i}_\mathrm{s}(t) \tag{2.4c}$$

where ψ_pm, $\underline{u}_\mathrm{s}$ and $\underline{i}_\mathrm{s}$ are the PM flux, voltage and current vectors in rotor coordinates. Using (2.3) and (2.4), the voltage equation (2.2) in rotor coordinates become

$$\frac{\mathrm{d}\underline{i}_\mathrm{s}(t)}{\mathrm{d}t} = \underline{a}_\mathrm{c}\underline{i}_\mathrm{s}(t) + b_\mathrm{c}\underline{u}_\mathrm{s}(t) + \underline{b}_{\psi\mathrm{c}}\psi_\mathrm{pm} \tag{2.5}$$

where

$$\underline{a}_\mathrm{c} = -\frac{R_\mathrm{s}}{L_\mathrm{s}} - \mathrm{j}\omega_\mathrm{m}, \quad b_\mathrm{c} = \frac{1}{L_\mathrm{s}}, \quad \underline{b}_{\psi\mathrm{c}} = -\frac{\mathrm{j}\omega_\mathrm{m}}{L_\mathrm{s}} \tag{2.6}$$

It can be seen from (2.5) and (2.6) that the back-emf term $\underline{b}_{\psi\mathrm{c}}\psi_\mathrm{pm}$ is constant if the speed of the motor is constant, as the PM flux is constant in rotor coordinates.

The electromagnetic torque of the machine is given by

$$T_\mathrm{e} = \frac{3p}{2}\,\mathrm{Im}\left\{\underline{\psi}_\mathrm{s}^*\underline{i}_\mathrm{s}\right\} \tag{2.7}$$

where p is the number of pole pairs and * represent the complex conjugate. The stator flux vector $\underline{\psi}_\mathrm{s}$ and the stator current vector $\underline{i}_\mathrm{s}$ are

$$\underline{\psi}_\mathrm{s} = L_\mathrm{s}\underline{i}_\mathrm{s} + \psi_\mathrm{pm}, \tag{2.8a}$$

$$\underline{i}_\mathrm{s} = i_\mathrm{d} + \mathrm{j}i_\mathrm{q} \tag{2.8b}$$

where i_d and i_q are the d- and q-components of the stator current $\underline{i}_\mathrm{s}$. Using the results from the above equation, (2.7) becomes

$$T_\mathrm{e} = \frac{3p}{2}\psi_\mathrm{pm} i_\mathrm{q} \tag{2.9}$$

It is clear from (2.9) that the electromagnetic torque only depends on the value of the q-axis current i_q, as the PM flux ψ_pm is constant in rotor coordinates. The equation of motion is given by

$$J\frac{d\omega_\mathrm{m}}{\mathrm{d}t} = T_\mathrm{e} - T_\mathrm{L} \tag{2.10}$$

where J is the total moment of inertia of the system and T_L is the load torque.

2.2 Discrete-Time Model of an SPMSM

Different approaches have been used in the literature to model the stator voltage when deriving discrete-time models for synchronous machines, considering the zero-order-hold (ZOH) in rotor coordinates [18, 20] or in stator coordinates [11, 14]. In the derivation of a discrete-time model for an SPMSM, following assumptions are used:

i. The rotor speed ω_m is assumed to be constant between the two consecutive sampling instants.

ii. Motor parameters ($R_\mathrm{s},\ L_\mathrm{s},\ \psi_\mathrm{pm}$) are assumed to be constant between the two sampling instants.

Sampling of the stator current is synchronized with the pulse-width modulation (PWM) and the switching-cycle averaged quantities are considered. Based on these assumptions, the stator voltage in stator coordinates is a piecewise constant between the two sampling instants and thus, corresponds to a ZOH in stator coordinates. It means that if k is the sampling instant and T_s is the sampling period, then the stator voltage $\underline{u}^\mathrm{s}_\mathrm{s}(t)$ is constant between two sampling instants, i.e., between $kT_\mathrm{s} < t < (k+1)T_\mathrm{s}$. From (2.11), it can be seen that the back-emf term $\underline{b}_{\psi\mathrm{c}}\psi_\mathrm{pm}$ is constant in rotor coordinates (if the rotor speed is constant). If the back-emf is represented in stator coordinates $\mathrm{j}\omega_\mathrm{m} e^{\mathrm{j}\omega_\mathrm{m} t}\psi_\mathrm{pm}$, it changes to a vector, rotating at a synchronous speed ω_m unless the rotor speed is zero.

The exact discrete-time model of an SPMSM can be found using (2.5) as described in [23]. The stator voltage $\underline{u}_\mathrm{s}(t)$ is considered in stator coordinates. From (2.5) we get

$$\frac{\mathrm{d}\underline{i}_\mathrm{s}(t)}{\mathrm{d}t} = \underline{a}_\mathrm{c}\underline{i}_\mathrm{s}(t) + \underline{b}^\mathrm{s}_\mathrm{c}\underline{u}^\mathrm{s}_\mathrm{s}(t) + \underline{b}_{\psi\mathrm{c}}\psi_\mathrm{pm} \tag{2.11}$$

where the time-varying input parameter is given by

$$\underline{b}_{\mathrm{c}}^{\mathrm{s}} = \frac{\mathrm{e}^{-\mathrm{j}\vartheta_{\mathrm{m}}(t)}}{L_{\mathrm{s}}} \tag{2.12}$$

If the rotor speed ω_{m} is assumed to be constant, the following relation for the angle $\vartheta_{\mathrm{m}}(t)$ will hold

$$\vartheta_{\mathrm{m}}(t) = \vartheta_{\mathrm{m}}(0) + \omega_{\mathrm{m}} t \tag{2.13}$$

where $\vartheta_{\mathrm{m}}(0)$ is the initial rotor angle.

2.2.1 ZOH in Rotor Coordinates

In this section, the ZOH of the stator voltage is assumed to be in rotor coordinates. The PWM signals are used to update the voltage pulses in stator coordinates. In a full digital implementation, usually one sampling period T_{s} is used for computational delay compensation. Furthermore, implementing a space-vector PWM in a digital domain introduces further delay in the system, which can be approximated as half a sampling period $0.5T_{\mathrm{s}}$ delay [20]. So, a total of $1.5T_{\mathrm{s}}$ delay is introduced in a digital domain when the ZOH of the stator voltage is assumed to be in rotor coordinates. The time delay $0.5T_{\mathrm{s}}$ results in a phase and magnitude error. An analytical solution to compensate the magnitude and phase errors was presented in [20]. The discrete-time model of an SPMSM becomes

$$\underline{i}_{\mathrm{s}}(k+1) = \underline{a}\,\underline{i}_{\mathrm{s}}(k) + \underline{b}'\,\underline{u}'_{\mathrm{s}}(k) + \underline{b}_{\psi}\psi_{\mathrm{pm}} \tag{2.14}$$

where $\underline{u}'_{\mathrm{s}}(k)$ is the uncompensated stator voltage and $\underline{a}$, $\underline{b}'$ and $\underline{b}_{\psi}$ are the complex parameters for the current, voltage and PM flux. The complex parameters used in (2.14) can be calculated as

$$\underline{a} = \mathrm{e}^{\underline{a}_{\mathrm{c}} T_{\mathrm{s}}} \tag{2.15a}$$

$$\underline{b}' = \int_0^{T_{\mathrm{s}}} \mathrm{e}^{\underline{a}_{\mathrm{c}}\tau}\mathrm{d}\tau \cdot \underline{b} = \underline{a}_{\mathrm{c}}^{-1}(\underline{a}-1)\underline{b} = \frac{1-\underline{a}}{R_{\mathrm{s}} + \mathrm{j}\omega_{\mathrm{m}} L_{\mathrm{s}}} \tag{2.15b}$$

$$\underline{b}_{\psi} = \int_0^{T_{\mathrm{s}}} \mathrm{e}^{\underline{a}_{\mathrm{c}}\tau}\mathrm{d}\tau \cdot \underline{b}_{\psi\mathrm{c}} = \frac{\mathrm{j}\omega_{\mathrm{m}}(\underline{a}-1)}{R_{\mathrm{s}} + \mathrm{j}\omega_{\mathrm{m}} L_{\mathrm{s}}} \tag{2.15c}$$

The one-step computational delay used to compensate the finite computation time of the control is usually considered as a delay in the stator voltage, in stator coordinates as

$$\underline{u}_{\mathrm{s}}^{\mathrm{s}}(k) = \underline{u}_{\mathrm{s,ref}}^{\mathrm{s}}(k-1) \tag{2.16a}$$

or, when transformed into rotor coordinates

$$\underline{u}_{\mathrm{s}}(k) = \mathrm{e}^{-\mathrm{j}\omega_{\mathrm{m}} T_{\mathrm{s}}} \underline{u}_{\mathrm{s,ref}}(k-1) \tag{2.16b}$$

where, $\underline{u}_{\mathrm{s,ref}}(k-1)$ is the one-step delayed output of the current regulator in rotor coordinates. Voltage vector in rotor coordinates is rotating at a synchronous speed ω_{m} and the one-sampling period delay introduces a phase error of $T_{\mathrm{s}}\omega_{\mathrm{m}}$ (where ω_{m}

is assumed to be a quasi-constant quantity – constant between the two consecutive sampling instants). This effect of the computational time delay on the voltage angle can be easily compensated in coordinate transformation. In order to simplify the equations, a simple change in notation is introduced here

$$\underline{u}'_{\mathrm{s,ref}} = \mathrm{e}^{-\mathrm{j}\omega_{\mathrm{m}}T_{\mathrm{s}}}\underline{u}_{\mathrm{s,ref}} \tag{2.17a}$$

which gives

$$\underline{u}_{\mathrm{s}}(k) = \underline{u}'_{\mathrm{s,ref}}(k-1) \tag{2.17b}$$

Furthermore, the angle compensation used for transforming the stator voltage from rotating to stationary coordinates is $\mathrm{e}^{\mathrm{j}\vartheta'_{\mathrm{m}}}$, where

$$\vartheta'_{\mathrm{m}} = \vartheta_{\mathrm{m}} + T_{\mathrm{s}}\omega_{\mathrm{m}} \tag{2.18}$$

As mentioned earlier, in a drive system, the converter output voltage is kept constant between the two sampling instants in stator coordinates. But as the ZOH of the stator voltage is assumed in rotor coordinates, the phase and magnitude errors produced in the stator voltage need to be compensated. Compensation for a purely inductive load is presented as [20]

$$\underline{u}'_{\mathrm{s}}(k) = \frac{\omega_{\mathrm{m}}T_{\mathrm{s}}/2}{\sin(\omega_{\mathrm{m}}T_{\mathrm{s}}/2)}\mathrm{e}^{-\mathrm{j}\omega_{\mathrm{m}}T_{\mathrm{s}}/2}\underline{u}_{\mathrm{s}}(k) \tag{2.19}$$

It should be noted that the magnitude compensation for high sampling frequencies (small sampling period T_{s}) reduce to unity. From basic trigonometry, if the angle $\omega_{\mathrm{m}}T_{\mathrm{s}}/2$ is small (in radians), which is the case if the sampling frequency is high, then

$$\sin(\theta) \approx \theta$$

From this approximation, (2.19) can be written as $\underline{u}'_{\mathrm{s}}(k) = \mathrm{e}^{-\mathrm{j}\omega_{\mathrm{m}}T_{\mathrm{s}}/2}\underline{u}_{\mathrm{s}}(k)$.

It is worth mentioning here that the switching-cycle averaged quantities neglect the switching harmonics produced by the PWM of power electronic switches. The effect of these switching harmonics is not included in the discrete-time design, as the current ripple produced by these harmonics is taken out due to the use of sampled feedback current signals [14].

2.2.2 ZOH in Stator Coordinates

In this section, the ZOH is assumed to be in stator coordinates, where it occurs naturally. This inherently takes into account the effect of time delay due to the ZOH. Using this assumption, the discrete-time model of an SPMSM is derived using (2.11) as a starting point, which can take the back-emf into account in rotor coordinates

$$\underline{i}_{\mathrm{s}}(k+1) = \underline{a}\,\underline{i}_{\mathrm{s}}(k) + \underline{b}\,\underline{u}_{\mathrm{s}}(k) + \underline{b}_{\psi}\psi_{\mathrm{pm}} \tag{2.20}$$

The complex parameters $\underline{a}$ and $\underline{b}_\psi$ are same as given in (2.15), where $\underline{b}$ can be calculated for an IPMSM as [5]

$$\underline{b} = \int_0^{T_\mathrm{s}} \mathrm{e}^{\underline{a}_\mathrm{c}\tau}\underline{b}_\mathrm{c}^\mathrm{s}(T_\mathrm{s}-\tau)\mathrm{d}\tau \cdot \mathrm{e}^{\mathrm{j}\vartheta_\mathrm{m}(0)} = \frac{\mathrm{e}^{-\mathrm{j}\omega_\mathrm{m}T_\mathrm{s}} - \underline{a}}{R_\mathrm{s}} \tag{2.21}$$

It should be noted that $\mathrm{e}^{\mathrm{j}\vartheta_\mathrm{m}(0)}$ used in $\underline{b}$ is the coordinate transformation from stationary to synchronous coordinates. The purpose behind this is to represent all the variables in rotor coordinate system.

2.3 Continuous-Time Model of an IPMSM

IPMSMs have magnets buried inside the rotor, increasing the effective air-gap and reducing the inductance in the d-axis (magnetic axis) direction compared with the q-axis. The conceptual diagram of an IPMSM is shown in Figure 2.3. The stator and rotor are shown in Figure 2.3 with PMs buried inside the rotor. The region between the stator and rotor is the air-gap. The d-axis is oriented in the direction of the PM flux and q-axis is orthogonal to the d-axis. Change in the air-gap in one direction makes the inductance position-dependent in stator coordinates.

The SyRM is a special case of an IPMSM with the PM flux equal to zero ($\psi_\mathrm{pm} = 0$). Therefore, the model of an IPMSM will be developed and it can be easily transformed to a SyRM by inserting ψ_pm equal to zero. Complex space vectors were used to model an SPMSM, but it is difficult to model IPMSMs or SyRMs using these complex space vectors. Instead of complex space vectors, real valued space vectors will be used. Space vectors and matrices will be presented with boldface letters. All the quantities in stator coordinates will have the superscript s. In rotor coordinates, the usual symbolic representation without any superscript is used.

Real space vectors and the inductance matrix in rotor coordinates are defined as

$$\boldsymbol{u}_\mathrm{s} = \begin{bmatrix} u_\mathrm{d} \\ u_\mathrm{q} \end{bmatrix}, \quad \boldsymbol{i}_\mathrm{s} = \begin{bmatrix} i_\mathrm{d} \\ i_\mathrm{q} \end{bmatrix}, \quad \boldsymbol{\psi}_\mathrm{s} = \begin{bmatrix} \psi_\mathrm{d} \\ \psi_\mathrm{q} \end{bmatrix} \tag{2.22}$$

$$\boldsymbol{\psi}_\mathrm{pm} = \begin{bmatrix} \psi_\mathrm{pm} \\ 0 \end{bmatrix}, \quad \boldsymbol{L}_\mathrm{s} = \begin{bmatrix} L_\mathrm{d} & 0 \\ 0 & L_\mathrm{q} \end{bmatrix}$$

Using (2.22) and (2.11) with the stator flux as a state variable we get the following voltage equation for an IPMSM

$$\frac{\mathrm{d}\boldsymbol{\psi}_\mathrm{s}(t)}{\mathrm{d}t} = \boldsymbol{A}_\mathrm{c}\boldsymbol{\psi}_\mathrm{s}(t) + \boldsymbol{B}_\mathrm{c}^\mathrm{s}(t)\boldsymbol{u}_\mathrm{s}^\mathrm{s}(t) + \boldsymbol{b}_\mathrm{c}\psi_\mathrm{pm} \tag{2.23}$$

where

$$\boldsymbol{A}_{\mathrm{c}} = \begin{bmatrix} -R_{\mathrm{s}}/L_{\mathrm{d}} & \omega_{\mathrm{m}} \\ -\omega_{\mathrm{m}} & -R_{\mathrm{s}}/L_{\mathrm{q}} \end{bmatrix}, \quad \boldsymbol{B}_{\mathrm{c}}^{\mathrm{s}}(t) = \mathrm{e}^{-\vartheta_{\mathrm{m}}(t)\boldsymbol{J}}, \quad \boldsymbol{b}_{\mathrm{c}} = \begin{bmatrix} R_{\mathrm{s}}/L_{\mathrm{d}} \\ 0 \end{bmatrix}, \tag{2.24}$$

and $\boldsymbol{J}$ is an orthogonal rotation matrix given by

$$\boldsymbol{J} = \begin{bmatrix} 0 & -1 \\ 1 & 0 \end{bmatrix} \tag{2.25}$$

The voltage input matrix in rotor coordinates is a 2×2 identity matrix

$$\boldsymbol{B}_{\mathrm{c}} = \boldsymbol{I} = \begin{bmatrix} 1 & 0 \\ 0 & 1 \end{bmatrix} \tag{2.26}$$

The stator-flux vector $\boldsymbol{\psi}_{\mathrm{s}}$ can be written as

$$\boldsymbol{\psi}_{\mathrm{s}}(t) = \boldsymbol{L}_{\mathrm{s}}\boldsymbol{i}_{\mathrm{s}}(t) + \boldsymbol{\psi}_{\mathrm{pm}} \tag{2.27}$$

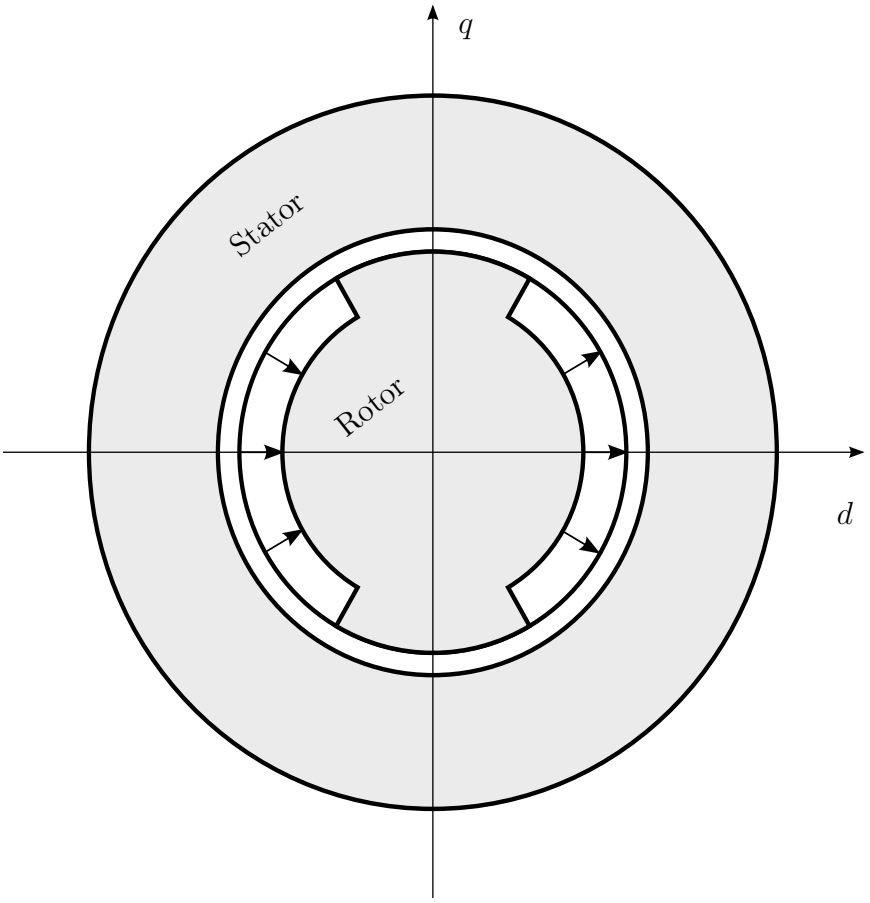

Figure 2.3: Conceptual diagram of an IPMSM (modified based on [22]).

Using (2.22), (2.23) and (2.27), the derivative of the stator flux in a component form can be written as follows

$$\begin{aligned}\frac{\mathrm{d}\psi_\mathrm{d}}{\mathrm{d}t} &= u_\mathrm{d} - R_\mathrm{s} i_\mathrm{d} + \omega_\mathrm{m}\psi_\mathrm{q} \\ \frac{\mathrm{d}\psi_\mathrm{q}}{\mathrm{d}t} &= u_\mathrm{d} - R_\mathrm{s} i_\mathrm{q} - \omega_\mathrm{m}\psi_\mathrm{d}\end{aligned} \tag{2.28}$$

where ψ_d and ψ_q are the d- and q-components of the stator flux $\boldsymbol{\psi}_\mathrm{s}$ given as

$$\begin{aligned}\psi_\mathrm{d} &= L_\mathrm{d} i_\mathrm{d} + \psi_\mathrm{pm} \\ \psi_\mathrm{q} &= L_\mathrm{q} i_\mathrm{q}\end{aligned} \tag{2.29}$$

If we replace $L_\mathrm{d} = L_\mathrm{q} = L_\mathrm{s}$, the equations (2.28) and (2.29) become the same as those for the case of an SPMSM. If we insert $\psi_\mathrm{pm} = 0$, the equations reduce to the model of a SyRM, which is a special case of an IPMSM. From (2.27), the current is given as

$$\boldsymbol{i}_\mathrm{s}(t) = \boldsymbol{C}\boldsymbol{\psi}_\mathrm{s}(t) + \boldsymbol{d}\psi_\mathrm{pm} \tag{2.30}$$

where

$$\boldsymbol{C} = \begin{bmatrix} 1/L_\mathrm{d} & 0 \\ 0 & 1/L_\mathrm{q} \end{bmatrix}, \quad \boldsymbol{d} = \begin{bmatrix} -1/L_\mathrm{d} \\ 0 \end{bmatrix} \tag{2.31}$$

The electromagnetic torque equation for an IPMSM can be found in a similar way as for an SPMSM. Using (2.7) for an IPMSM, we get

$$T_\mathrm{e} = \frac{3p}{2}\Big(\psi_\mathrm{d} i_\mathrm{q} - \psi_\mathrm{q} i_\mathrm{d}\Big) = \frac{3p}{2}\Big[\psi_\mathrm{pm} i_\mathrm{q} + (L_\mathrm{d} - L_\mathrm{q}) i_\mathrm{d} i_\mathrm{q}\Big] \tag{2.32}$$

From the above equation, it is clear that there is an extra term $(L_\mathrm{d} - L_\mathrm{q}) i_\mathrm{d} i_\mathrm{q}$ compared with the case of an SPMSM given in (2.9). The term $\frac{3p}{2}(L_\mathrm{d} - L_\mathrm{q}) i_\mathrm{d} i_\mathrm{q}$ is called the reluctance torque and is produced due to the saliency of the machine. If we select the value of $L_\mathrm{d} = L_\mathrm{q}$ in (2.32), we get (2.9) which is the torque equation for an SPMSM. Furthermore, if the saliency $L_\mathrm{d} - L_\mathrm{q}$ is large, the torque production can be maximized by using a non-zero value of i_d. The PM flux is absent in the case of a SyRM. From (2.32) it can be seen that there will still be torque even if the value of $\psi_\mathrm{pm} = 0$. This reluctance torque is the basis of calling this type of machine a synchronous reluctance motor.

2.4 Discrete-Time Models of an IPMSM

The continuous-time design is a well-established and understood design approach. Usually the continuous-time model of a plant is available and the controller is designed based on this model. The continuous-time designed controllers are then discretized using the Euler or Tustin approximations for digital implementation in the emulation-based design. The emulation-based controllers work well with digital

processors if the sampling frequency is high enough compared with the excitation frequency. In order to improve the controller performance, the exact discrete-time model of the plant is needed.

Exact discrete-time models can be computationally demanding. An approximate solution could be used instead to improve the computational efficiency. The textbook approach to find the approximate discrete-time models is to use a series expansion of the exact discrete-time matrices, as given in [23]. First, the exact discrete-time model of an IPMSM is presented, then, the approximate solutions based on series expansions are obtained.

2.4.1 Exact Discrete-Time Model

The exact discrete-time model of an IPMSM can be found based on the assumptions made for the case of an SPMSM.

The ZOH of the stator voltage is assumed to be in stator coordinates. Sampling of the stator current is synchronized with the pulse-width modulation (PWM) and the switching cycle averaged quantities are considered. Furthermore, the sampling and the switching frequencies are equal. It should be noted that the ZOH in stator coordinates means that the stator voltage is a piecewise constant in stator coordinates. It means that the stator voltage remains constant between the two consecutive sampling instants, i.e., $\boldsymbol{u}_\mathrm{s}^\mathrm{s}(t)$ is constant during $kT_\mathrm{s} < t < (k+1)T_\mathrm{s}$, where T_s is the sampling period and k is the discrete-time index. The discrete-time model for an IPMSM becomes

$$\boldsymbol{\psi}_\mathrm{s}(k+1) = \boldsymbol{A}_\mathrm{d}\boldsymbol{\psi}_\mathrm{s}(k) + \boldsymbol{B}_\mathrm{d}\boldsymbol{u}_\mathrm{s}(k) + \boldsymbol{b}_\mathrm{d}\psi_\mathrm{pm} \tag{2.33a}$$

$$\boldsymbol{i}_\mathrm{s}(k) = \boldsymbol{C}\boldsymbol{\psi}_\mathrm{s}(k) + \boldsymbol{d}\psi_\mathrm{pm} \tag{2.33b}$$

where the discrete-time matrices in (2.33) can be found as in [5].

The system matrix is

$$\boldsymbol{A}_\mathrm{d} = \mathrm{e}^{\boldsymbol{A}_\mathrm{c}T_\mathrm{s}} = \begin{bmatrix} a_\mathrm{d11} & a_\mathrm{d12} \\ a_\mathrm{d21} & a_\mathrm{d22} \end{bmatrix} \tag{2.34}$$

The input matrix $\boldsymbol{B}_\mathrm{c}^\mathrm{s}(t)$ corresponding to the stator voltage is time-varying in stator coordinates. Hence, the discrete-time input matrix becomes

$$\boldsymbol{B}_\mathrm{d} = \int_0^{T_\mathrm{s}} \mathrm{e}^{\boldsymbol{A}_\mathrm{c}\tau}\boldsymbol{B}_\mathrm{c}^\mathrm{s}(T_\mathrm{s}-\tau)\mathrm{d}\tau \cdot \mathrm{e}^{\vartheta_\mathrm{m}(0)\boldsymbol{J}} = \begin{bmatrix} b_\mathrm{d11} & b_\mathrm{d12} \\ b_\mathrm{d21} & b_\mathrm{d22} \end{bmatrix} \tag{2.35}$$

where $\mathrm{e}^{\vartheta_\mathrm{m}(0)\boldsymbol{J}}$ is the coordinate transformation from stator to rotor coordinates.

The input matrix corresponding to the PM flux is

$$\boldsymbol{b}_\mathrm{d} = \int_0^{T_\mathrm{s}} \mathrm{e}^{\boldsymbol{A}_\mathrm{c}\tau}\mathrm{d}\tau \cdot \boldsymbol{b}_\mathrm{c} = \begin{bmatrix} b_\mathrm{d1} \\ b_\mathrm{d2} \end{bmatrix} \tag{2.36}$$

The elements of matrices $\boldsymbol{A}_\mathrm{d}, \boldsymbol{B}_\mathrm{d}$ and $\boldsymbol{b}_\mathrm{d}$ can be found in Appendix A.

Using the stator current as a state variable, the state equation becomes

$$\boldsymbol{i}_\mathrm{s}(k+1) = \boldsymbol{A}\boldsymbol{i}_\mathrm{s}(k) + \boldsymbol{B}\boldsymbol{u}_\mathrm{s}(k) + \boldsymbol{b}\psi_\mathrm{pm} \tag{2.37}$$

where

$$\boldsymbol{A} = \boldsymbol{C}\boldsymbol{A}_\mathrm{d}\boldsymbol{C}^{-1} = \begin{bmatrix} a_\mathrm{d11} & \frac{L_\mathrm{q}}{L_\mathrm{d}}a_\mathrm{d12} \\ \frac{L_\mathrm{d}}{L_\mathrm{q}}a_\mathrm{d21} & a_\mathrm{d22} \end{bmatrix} \tag{2.38a}$$

$$\boldsymbol{B} = \boldsymbol{C}\boldsymbol{B}_\mathrm{d} = \begin{bmatrix} \frac{b_\mathrm{d11}}{L_\mathrm{d}} & \frac{b_\mathrm{d12}}{L_\mathrm{d}} \\ \frac{b_\mathrm{d21}}{L_\mathrm{q}} & \frac{b_\mathrm{d22}}{L_\mathrm{q}} \end{bmatrix} \tag{2.38b}$$

$$\boldsymbol{b} = (\boldsymbol{I} - \boldsymbol{A})\boldsymbol{d} + \boldsymbol{C}\boldsymbol{b}_\mathrm{d} = \begin{bmatrix} \frac{a_\mathrm{d11}+b_\mathrm{d1}-1}{L_\mathrm{d}} \\ \frac{a_\mathrm{d21}+b_\mathrm{d2}}{L_\mathrm{q}} \end{bmatrix} \tag{2.38c}$$

2.4.2 Approximation of the Exact Discrete-Time Model

The approximate solution for the exact discrete-time matrices in (2.33) can be found using series expansions given in [23]. The system matrix $\boldsymbol{A}_\mathrm{d}$ can be expressed as

$$\boldsymbol{A}_\mathrm{d} = \boldsymbol{I} + T_\mathrm{s}\boldsymbol{A}_\mathrm{c}\boldsymbol{F} \tag{2.39}$$

where

$$\boldsymbol{F} = \boldsymbol{I} + \frac{T_\mathrm{s}\boldsymbol{A}_\mathrm{c}}{2!} + \frac{T_\mathrm{s}^2\boldsymbol{A}_\mathrm{c}^2}{3!} + \ldots \tag{2.40}$$

From (2.35) it can be seen that the voltage input matrix is a time-varying matrix and it is difficult to express it directly in a series expansion form. If the ZOH is assumed in rotor coordinates instead of stator coordinates, the voltage input matrix can be written as

$$\boldsymbol{B}_\mathrm{d} \approx T_\mathrm{s}\boldsymbol{F}\boldsymbol{B}_\mathrm{c} \tag{2.41}$$

As explained earlier, if the ZOH is assumed to be in rotor coordinates, the voltage input matrix is changed according to the compensation made in [20]. Using (2.19) for an IPMSM, the voltage input matrix becomes

$$\boldsymbol{B}_\mathrm{d} \approx T_\mathrm{s}\boldsymbol{F}\boldsymbol{B}_\mathrm{c}\frac{\omega_\mathrm{m}T_\mathrm{s}/2}{\sin(\omega_\mathrm{m}T_\mathrm{s}/2)}e^{-(\omega_\mathrm{m}T_\mathrm{s}/2)\boldsymbol{J}} \tag{2.42}$$

From (2.36) it is clear that there is no time-varying component in the PM flux input matrix, as the PM flux is constant in rotor coordinates. So, the matrix $\boldsymbol{b}_\mathrm{d}$ can be written as

$$\boldsymbol{b}_\mathrm{d} = T_\mathrm{s}\boldsymbol{F}\boldsymbol{b}_\mathrm{c} \tag{2.43}$$

As the sampling period T_s usually has a small value, only one or two terms of (2.40) are used, i.e., $\boldsymbol{F} = \boldsymbol{I}$ or $\boldsymbol{F} = \boldsymbol{I} + (T_\mathrm{s}/2)\boldsymbol{A}_\mathrm{c}$. Using $\boldsymbol{F} = \boldsymbol{I}$ corresponds to the forward Euler discretization of the continuous-time motor model.

Chapter 3

Current Control Methods

The field oriented control with the reference frame fixed to the rotor is used for the control of AC motors. In a rotor fixed reference frame, both the flux and the electromagnetic torque can be controlled separately by controlling the respective components (i_{d} and i_{q}) of the stator current. This type of control resembles the control of DC motors [15]. Vector control methods based on the dynamic models of electric motors are generally used if high accuracy and fast dynamics are required. The vector control of a synchronous motor requires the rotor position, which can be measured using a mechanical position sensor mounted on the shaft of a motor or estimated using a flux observer.

3.1 Stability of a Linear Control System

Stability is the most fundamental property of a feedback control system. It can be considered as a starting point in determining the performance of a control system. One way to define the stability of a linear system is using an impulse response of the system. If the impulse response of a linear control system approaches zero or is limited (bounded) as the time approaches infinity, the system is stable, otherwise unstable. Further details about the stability analysis of a linear control system can be found in [24] and [25].

From the basic control theory, it is clear that the stable region of the s-plane is mapped onto a unit disc in the z-plane. Suppose a system matrix of an overall control system (including the motor and controller) is represented by $\mathbf{\Phi}$. The eigenvalues of this system matrix represent the poles of the system. Let us suppose that $\lambda_1, \lambda_2, \ldots, \lambda_N$ represent the eigenvalues of the system matrix $\mathbf{\Phi}$, then the conditions for stability are as follows:

i. **Asymptotic stability:** The magnitude of the eigenvalues (λ_i) of a system matrix is less than 1. It means that all the eigenvalues of a system are inside the unit disc in the z-plane.

ii. **Marginal stability:** If there is an eigenvalue with magnitude 1, this will make the system marginally or conditionally stable.

iii. **Unstable:** If there is even a single eigenvalue with magnitude greater than 1 (outside the unit disc), this will make the system unstable.

3.2 State of the Art Controllers

The internal model control (IMC) method to design a synchronous-frame proportional integral (PI) current controller can be considered as a state of the art controller [7]. In this type of controller, a trial and error phase of selecting the proportional gain and integration time constant is removed. The controller parameters are based on the motor model and desired controller bandwidth. This method works very well for IMs and SPMSMs but it is not suitable for IPMSMs and SyRMs running at high rotor speeds.

Cross-coupling between the d- and q-axis current components exists in a model-based synchronous-frame PI-type current controller. A transient error is produced in the d-axis current whenever there is a step change in a reference value of the q-axis current and vice versa. In order to reduce the transient error, different improvements have been proposed for the synchronous-frame PI-type controller, one of them is based on a one-step predicted current [18]. During steady state there are high frequency oscillations in the d- and q-axis current components. These oscillations can be reduced by introducing a one-step predicted current in the decoupling terms of the controller. Furthermore, the one-step predicted current is also introduced in the damping term (active resistance) to reduce the level of oscillations. The complex PI-type controller gives better performance with one-step predicted compensation [18].

Some other controllers used in the current control of AC motors are the hysteresis controller, stator-frame PI controller, state-feedback controller, predictive and dead-beat direct torque controllers [18, 26, 27]. The hysteresis controller is simple but the switching frequency is not constant unlike in the case of the synchronous-frame PI-type controller. The steady state error is zero in synchronous-frame PI-type controller unlike the stator frame PI-type controller. The predictive and dead beat controllers are sensitive to parameter errors [18]. The synchronous-frame PI-type controller is a special case of the state feedback controller with integral action.

The one-step prediction algorithm with the forward Euler approximation used in a synchronous-frame PI-type controller for the current control of an IPMSM is

given below [18]

$$\boldsymbol{\psi}_{\mathrm{s}}(k) = \boldsymbol{L}_{\mathrm{s}}\boldsymbol{i}_{\mathrm{s}}(k) + \boldsymbol{\psi}_{\mathrm{pm}} \tag{3.1a}$$

$$\boldsymbol{\psi}_{\mathrm{s}}(k+1) = \boldsymbol{\psi}_{\mathrm{s}}(k) + T_{\mathrm{s}}\big[\boldsymbol{u}_{\mathrm{s}}(k) - R_{\mathrm{s}}\boldsymbol{i}_{\mathrm{s}}(k) - \omega_{\mathrm{m}}\boldsymbol{J}\boldsymbol{\psi}_{\mathrm{s}}(k)\big] \tag{3.1b}$$

$$\boldsymbol{i}_{\mathrm{s}}(k+1) = \boldsymbol{C}\boldsymbol{\psi}_{\mathrm{s}}(k+1) + \boldsymbol{d}\psi_{\mathrm{pm}} \tag{3.1c}$$

It should be noted that the present value of the stator flux $\boldsymbol{\psi}_{\mathrm{s}}(k)$ is calculated based on the present value of the sampled stator current $\boldsymbol{i}_{\mathrm{s}}(k)$. A more detailed comparative study of the predictive current control schemes for PMSMs can be found in [28]. A predictive current control based on the forward Euler discretization of the continuous-time model of PMSMs can be found in [29, 30]. The performance of the predictive current controller deteriorates if there are parameter errors. The variation of parameters was compensated using a disturbance observer in [30]. A discrete-time PI-type current regulator for a SyRM running at high rotor speeds was presented in [31]. The controller gains were trial and error based, making the control specific to a particular machine.

First the continuous-time (2DOF) PI-type controller will be designed for SPMSMs, then a discrete-time 2DOF state-space controller will be developed. The results will then be extended for IPMSMs and SyRMs. Finally, the controller gains will be calculated for different approximate motor models described in Chapter 2.

3.3 Continuous-Time Design

The continuous-time designed controller works very well for symmetric machines with large ratios between the sampling and fundamental frequencies (at least 10). If the ratio between the sampling and excitation frequencies is small, the cross-coupling between the d- and q-axis becomes significant and the performance of the controller deteriorates.

The state-space controller with an integral action, reference feedforward and state feedback is used as a starting point for the control design. In rotor coordinates, the control law for SPMSMs in the Laplace domain can be expressed as follows

$$\underline{u}_{\mathrm{s,ref}}(s) = \underline{k}_{\mathrm{tc}}\underline{i}_{\mathrm{s,ref}}(s) + \frac{\underline{k}_{\mathrm{ic}}}{s}\big[\underline{i}_{\mathrm{s,ref}}(s) - \underline{i}_{\mathrm{s}}(s)\big] - \underline{k}_{\mathrm{1c}}\underline{i}_{\mathrm{s}}(s) \tag{3.2}$$

where $\underline{u}_{\mathrm{s,ref}}$ is the reference voltage, $\underline{i}_{\mathrm{s,ref}}$ is the reference current, $\underline{k}_{\mathrm{tc}}$ is the feedforward gain, $\underline{k}_{\mathrm{ic}}$ is the integral gain and $\underline{k}_{\mathrm{1c}}$ is the state feedback gain. For simplicity, an ideal voltage production with no time delays is considered, i.e., $\underline{u}_{\mathrm{s}} = \underline{u}_{\mathrm{s,ref}}$. Using (2.5) and (3.2) in the Laplace domain, we get

$$\underline{i}_{\mathrm{s}}(s) = \frac{\frac{\underline{k}_{\mathrm{tc}}}{L_{\mathrm{s}}}s + \frac{\underline{k}_{\mathrm{ic}}}{L_{\mathrm{s}}}}{s^2 + s\big(\frac{\underline{k}_{\mathrm{1c}}}{L_{\mathrm{s}}} - \underline{a}_{\mathrm{c}}\big) + \frac{\underline{k}_{\mathrm{ic}}}{L_{\mathrm{s}}}}\underline{i}_{\mathrm{s,ref}}(s) - \mathrm{j}\omega_{\mathrm{m}}\psi_{\mathrm{pm}}\frac{s/L_{\mathrm{s}}}{s^2 + s\big(\frac{\underline{k}_{\mathrm{1c}}}{L_{\mathrm{s}}} - \underline{a}_{\mathrm{c}}\big) + \frac{\underline{k}_{\mathrm{ic}}}{L_{\mathrm{s}}}} \tag{3.3}$$

The closed-loop current response becomes

$$\underline{i}_{\mathrm{s}}(s) = \underline{G}_{\mathrm{c}}(s)\underline{i}_{\mathrm{s,ref}}(s) - \underline{Y}_{\mathrm{ic}}(s)\underline{u}_{\mathrm{i}}(s) \tag{3.4}$$

where $\underline{u}_{\mathrm{i}} = \mathrm{j}\omega_{\mathrm{m}}\psi_{\mathrm{pm}}$ is the back-emf voltage, $\underline{G}_{\mathrm{c}}(s)$ and $\underline{Y}_{\mathrm{ic}}(s)$ are the closed-loop transfer functions for the reference following and the disturbance, respectively. It is worth noticing that, instead of considering $\underline{u}_{\mathrm{i}}$ as a state input, it can be seen as a disturbance input to the system. The closed-loop transfer functions are

$$\underline{G}_{\mathrm{c}}(s) = \frac{\underline{b}_{1\mathrm{c}}s + \underline{b}_{0\mathrm{c}}}{s^2 + \underline{a}_{1\mathrm{c}}s + \underline{a}_{0\mathrm{c}}} \tag{3.5}$$

$$\underline{Y}_{\mathrm{ic}}(s) = \frac{s/L_{\mathrm{s}}}{s^2 + \underline{a}_{1\mathrm{c}}s + \underline{a}_{0\mathrm{c}}} \tag{3.6}$$

respectively. The coefficients can be found using (3.3) as follows

$$\begin{aligned} \underline{a}_{0\mathrm{c}} = \underline{k}_{\mathrm{ic}}/L_{\mathrm{s}}, \quad \underline{a}_{1\mathrm{c}} = \underline{k}_{1\mathrm{c}}/L_{\mathrm{s}} - \underline{a}_{\mathrm{c}} \\ \underline{b}_{0\mathrm{c}} = \underline{a}_{0\mathrm{c}}, \quad \underline{b}_{1\mathrm{c}} = \underline{k}_{\mathrm{tc}}/L_{\mathrm{s}} \end{aligned} \tag{3.7}$$

Using these relations, the closed-loop poles and zeros can be placed easily

$$\underline{k}_{\mathrm{tc}} = \underline{b}_{1\mathrm{c}\star}\hat{L}_{\mathrm{s}}, \quad \underline{k}_{\mathrm{ic}} = \underline{a}_{0\mathrm{c}\star}\hat{L}_{\mathrm{s}}, \quad \underline{k}_{1\mathrm{c}} = (\underline{a}_{1\mathrm{c}\star} + \hat{\underline{a}}_{\mathrm{c}})\hat{L}_{\mathrm{s}} \tag{3.8}$$

where the parameter estimates are marked by the hat and the intended coefficients are marked by the subscript $\star$.

3.3.1 Synchronous-Frame 2DOF PI-Type Controller

The synchronous-frame PI controller parameters can be found by placing the two real poles using the characteristic polynomial of (3.5). The characteristic polynomial can be expressed as $s^2 + 2\zeta\omega_0 s + \omega_0^2$, where ω_0 is the undamped angular frequency and ζ is the damping ratio. By comparing a standard characteristic polynomial with the denominator of (3.5), the coefficients become $a_{0\mathrm{c}\star} = \omega_0^2$ and $a_{1\mathrm{c}\star} = 2\zeta\omega_0$ and for a stable system $\zeta > 0$. Hence, the design parameters for two real poles become

$$\underline{a}_{0\mathrm{c}\star} = \alpha^2, \quad \underline{a}_{1\mathrm{c}\star} = 2\alpha, \quad \underline{b}_{1\mathrm{c}\star} = \alpha \tag{3.9}$$

where α is the desired closed-loop control bandwidth. Using (3.9), the gains for the state-space controller given in (3.8) become

$$\underline{k}_{\mathrm{tc}} = \alpha\hat{L}_{\mathrm{s}} \tag{3.10a}$$

$$\underline{k}_{\mathrm{ic}} = \alpha^2\hat{L}_{\mathrm{s}} \tag{3.10b}$$

$$\underline{k}_{1\mathrm{c}} = 2\alpha\hat{L}_{\mathrm{s}} - \hat{R}_{\mathrm{s}} - \mathrm{j}\omega_{\mathrm{m}}\hat{L}_{\mathrm{s}} \tag{3.10c}$$

Using the design parameters of (3.9) in (3.2), the resulting equation corresponds to the 2DOF PI-type current controller given in [7,21,32,33]. The reference voltage in (3.2) becomes

$$\underline{u}_{\mathrm{s,ref}}(s) = \left(\alpha\hat{L}_{\mathrm{s}} + \frac{\alpha^2\hat{L}_{\mathrm{s}}}{s}\right)\left[\underline{i}_{\mathrm{s,ref}}(s) - \underline{i}_{\mathrm{s}}(s)\right] - \left(\alpha\hat{L}_{\mathrm{s}} - \hat{R}_{\mathrm{s}} - \mathrm{j}\omega_{\mathrm{m}}\hat{L}_{\mathrm{s}}\right)\underline{i}_{\mathrm{s}}(s) \tag{3.11}$$

From (3.5), (3.6) and (3.9), the closed-loop transfer functions for the reference following and disturbance rejection become

$$\underline{G}_{\mathrm{c}\star}(s) = \frac{\alpha(s+\alpha)}{(s+\alpha)^2} = \frac{\alpha}{s+\alpha} \tag{3.12a}$$

$$\underline{Y}_{\mathrm{ic}\star}(s) = \frac{s/L_{\mathrm{s}}}{(s+\alpha)^2} \tag{3.12b}$$

where the accurate parameter estimates have been assumed. It can be seen that the closed-loop pole in $\underline{G}_{\mathrm{c}\star}(s)$ is cancelled with a closed-loop zero.

It should be noted that a standard PI-type controller is tuned using two parameters, i.e., proportional and integral gain. The control law given in (3.11) has an advantage of tuning only one parameter, i.e., α [7]. Other parameters needed for the control are the motor parameters, which can be measured easily. However, the performance of this type of controller deteriorates as the ratio between the sampling and excitation frequencies decreases. This is due to the cross-coupling between the d- and q-axis quantities, which leads to oscillations and even instability of the system. In order to reduce the cross-coupling at low sampling to excitation (fundamental) frequency ratios, a one-step predicted current given in (3.1) can be used in the damping and cross-coupling terms.

3.3.2 Complex 2DOF PI-Type Controller

The complex vector design reduces sensitivity to parameter mismatch [8]. The design parameters for a complex PI-type controller were proposed in [8], [9] as follows

$$\underline{a}_{0\mathrm{c}\star} = (\alpha + \mathrm{j}\omega_{\mathrm{m}})\alpha, \quad \underline{a}_{1\mathrm{c}\star} = 2\alpha + \mathrm{j}\omega_{\mathrm{m}}, \quad \underline{b}_{1\mathrm{c}\star} = \alpha \tag{3.13}$$

where α is the current controller bandwidth and ω_{m} is the rotor speed. It should be noted that the estimated or measured motor parameters are needed for the controller parameter calculations. Using the actual motor parameters and the design parameters given in (3.13), the closed-loop transfer functions for the reference following and disturbance rejection become

$$\underline{G}_{\mathrm{c}\star}(s) = \frac{\alpha(s+\alpha+\mathrm{j}\omega_{\mathrm{m}})}{(s+\alpha)(s+\alpha+\mathrm{j}\omega_{\mathrm{m}})} = \frac{\alpha}{s+\alpha} \tag{3.14a}$$

$$\underline{Y}_{\mathrm{ic}\star}(s) = \frac{s/L_{\mathrm{s}}}{(s+\alpha)(s+\alpha+\mathrm{j}\omega_{\mathrm{m}})} \tag{3.14b}$$

It can be seen that the reference-following transfer function $\underline{G}_{\mathrm{c}\star}(s)$ is equal to the transfer function given in (3.12). From (3.14), it can be seen that the closed-loop system has one real pole and one complex pole $\big[$which is cancelled by the corresponding complex zero in $\underline{G}_{\mathrm{c}\star}(s)\big]$.

3.4 Discrete-Time Design

A 2DOF state-space controller shown in Figure 3.1 will be used for the design of a control scheme in the discrete-time domain for IPMSMs and SyRMs. The output voltage of the current regulator is used as a one-step delayed input to the controller. The reason for using the output voltage as a one-step delayed input is to directly place the poles and zero in the z-plane (discrete-time domain). Furthermore, the gains of the controller can be calculated using the estimated motor parameters ($\hat{R}_\mathrm{s},\ \hat{L}_\mathrm{d},\ \hat{L}_\mathrm{q}$) and the desired bandwidth α of the current controller.

It can be seen from Figure 3.1 that the plant model includes the coordinate transformation and the time delay (computational delay in the discrete-time domain). The angular error due to the computational time delay is compensated in the coordinate transformation of the stator voltage reference from rotor to stator coordinates, i.e.,

$$\vartheta'_\mathrm{m} = \vartheta_\mathrm{m} + T_\mathrm{s}\omega_\mathrm{m} \tag{3.15}$$

It should be noted that the angle compensation is only required in voltage transformation, no angular compensation is required for the current (stator to rotor transformation). The controller gains $\boldsymbol{K}_1$, $\boldsymbol{K}_2$, $\boldsymbol{K}_\mathrm{i}$, and $\boldsymbol{K}_\mathrm{t}$ are generally 2×2 matrices for IPMSMs and SyRMs, while they can be expressed as complex scalars ($\underline{k}_1$, $\underline{k}_2$, $\underline{k}_\mathrm{i}$, and $\underline{k}_\mathrm{t}$) in the case of an SPMSM. Furthermore, the sampling of the stator current $\boldsymbol{i}^\mathrm{s}_\mathrm{s}$ is synchronized with the PWM. For the position of the rotor (ϑ_m), a mechanical position sensor is used.

The rest of the chapter addresses the design of a discrete-time controller shown in Figure 3.1 and finding the gains of the controller using the discrete-time models of an SPMSM, IPMSM and SyRM given in Chapter 2. First the controller gains will be calculated using the discrete-time models of an SPMSM to reduce the complexity and then the results will be extended for more complex cases like IPMSMs and SyRMs.

The discrete-time counterpart of the control law given in (3.2) will be developed. The closed-loop transfer function for the control law given in (3.2) corresponds to a unity-gain first-order low pass filter

$$\frac{\underline{i}_\mathrm{s}(s)}{\underline{i}_\mathrm{s,ref}(s)} = \frac{\alpha}{s+\alpha} \tag{3.16}$$

In a digital domain, one-step computational time delay cannot be avoided. It can be modelled as $1/z$ in the z-domain. Mapping a real pole in the s-plane to z-plane changes it to exponential, i.e., $s = -\alpha$ becomes $z = \mathrm{e}^{-\alpha T_\mathrm{s}}$, where T_s is the sampling period. The closed-loop transfer function (3.16) with one-step delay in a digital domain (z-plane) become

$$\frac{\underline{i}_\mathrm{s}(z)}{\underline{i}_\mathrm{s,ref}(z)} = \frac{1-p_{1\star}}{z(z-p_{1\star})} \tag{3.17}$$

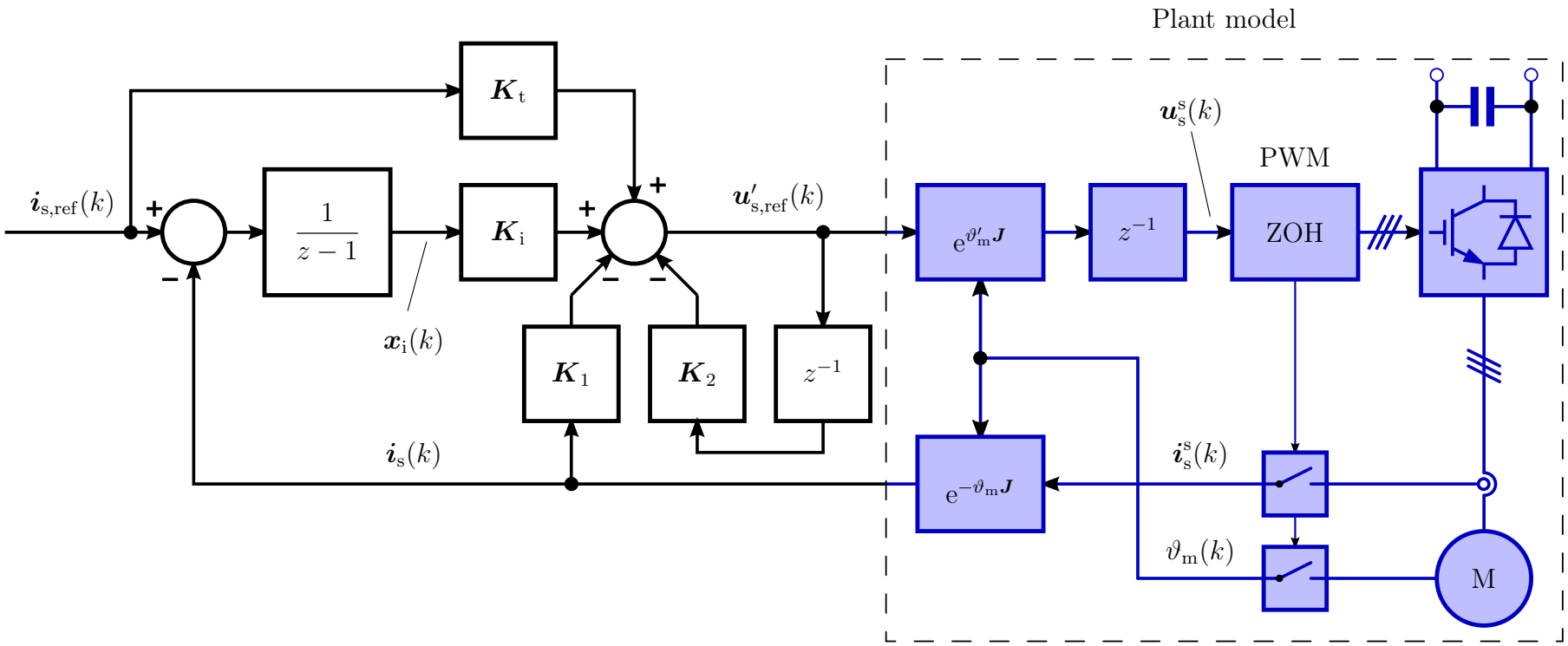

Figure 3.1: 2DOF state-space current controller with an integral action

where

$$p_{1\star} = \mathrm{e}^{-\alpha T_\mathrm{s}} \tag{3.18}$$

is the intended real pole of the system. It can be seen from (3.17) that as the transfer function is real valued, no cross-coupling between the axes exists.

Using the discrete-time transfer function in (3.17), the gains of the controller given in Figure 3.1 will be calculated, first for an SPMSM and then for an IPMSM and SyRM.

3.4.1 Current Control of an SPMSM

From Figure 3.1, the control law for an SPMSM in a digital domain using complex scalars can be written as

$$\underline{x}_\mathrm{i}(k+1) = \underline{x}_\mathrm{i}(k) + \underline{i}_{\mathrm{s,ref}}(k) - \underline{i}_\mathrm{s}(k) \tag{3.19a}$$

$$\underline{u}'_{\mathrm{s,ref}}(k) = \underline{k}_\mathrm{t}\underline{i}_{\mathrm{s,ref}}(k) + \underline{k}_\mathrm{i}\underline{x}_\mathrm{i}(k) - \underline{k}_1\underline{i}_\mathrm{s}(k) - \underline{k}_2\underline{u}_\mathrm{s}(k) \tag{3.19b}$$

where $\underline{x}_\mathrm{i}$ is the integral state, $\underline{k}_\mathrm{i}$ is the integral gain, $\underline{k}_\mathrm{t}$ is the feedforward gain, $\underline{k}_1$ and $\underline{k}_2$ are the state-feedback gains and $\underline{u}'_{\mathrm{s,ref}}(k)$ is the next step voltage i.e. $\underline{u}_\mathrm{s}(k+1) = \underline{u}'_{\mathrm{s,ref}}(k)$. Since all the states are directly available, the closed-loop poles can be placed arbitrarily. The control law (3.19) can be expressed in the z-domain as follows

$$\underline{u}'_{\mathrm{s,ref}}(z) = \underline{k}_\mathrm{t}\underline{i}_{\mathrm{s,ref}}(z) + \frac{\underline{k}_\mathrm{i}}{z-1}\left[\underline{i}_{\mathrm{s,ref}}(z) - \underline{i}_\mathrm{s}(z)\right] - \underline{k}_1\underline{i}_\mathrm{s}(z) - \frac{\underline{k}_2}{z}\underline{u}'_{\mathrm{s,ref}}(z) \tag{3.20}$$

The forward Euler approximation of a 2DOF PI controller given in (3.11) can be found if we select the following gains in (3.20)

$$\underline{k}_\mathrm{t} = k_\mathrm{pc}, \quad \underline{k}_\mathrm{i} = T_\mathrm{s}k_\mathrm{ic}, \quad \underline{k}_2 = 0 \tag{3.21}$$
$$\underline{k}_1 = k_\mathrm{pc} + R_\mathrm{a} - \mathrm{j}\omega_\mathrm{m}\hat{L}_\mathrm{s}$$

where

$$k_\mathrm{pc} = \alpha\hat{L}_\mathrm{s}, \quad k_\mathrm{ic} = \alpha^2\hat{L}_\mathrm{s} \tag{3.22}$$

As mentioned earlier, the performance of this type of controller deteriorates as the frequency ratio becomes lower than 20 between the sampling and fundamental frequencies [5].

For control purposes, the plant model in (2.20) can be written as follows

$$\begin{bmatrix} \underline{i}_\mathrm{s}(k+1) \\ \underline{u}_\mathrm{s}(k+1) \end{bmatrix} = \begin{bmatrix} \underline{a} & \underline{b} \\ 0 & 0 \end{bmatrix} \begin{bmatrix} \underline{i}_\mathrm{s}(k) \\ \underline{u}_\mathrm{s}(k) \end{bmatrix} + \begin{bmatrix} 0 \\ 1 \end{bmatrix} \underline{u}'_{\mathrm{s,ref}}(k) + \begin{bmatrix} \underline{b}_\psi \\ 0 \end{bmatrix} \psi_\mathrm{pm} \tag{3.23}$$

It should be noted that the time delay due to the ZOH is included in the plant model (when deriving the expression for $\underline{b}$) in a similar way as in [5]. The states $\underline{i}_\mathrm{s}$ and $\underline{u}_\mathrm{s}$

in the state feedback control are readily available as feedback signals. The stator current $\underline{i}_\mathrm{s}$ is available as a measured feedback signal and the stator voltage $\underline{u}_\mathrm{s}$ equals the previous value of the reference voltage $\underline{u}'_\mathrm{s,ref}$ (output of the current regulator). In a z-domain, the plant model (3.23) can be expressed as

$$\underline{i}_\mathrm{s}(z) = \underline{Y}(z)\underline{u}'_\mathrm{s,ref}(z) - \underline{Y}_\mathrm{d}(z)\underline{u}_\mathrm{i}(z) \tag{3.24}$$

where the pulse-transfer functions for the reference following and the load-disturbance rejection are

$$\underline{Y}(z) = \frac{\underline{b}}{z(z-\underline{a})}, \quad \underline{Y}_\mathrm{d}(z) = \frac{1}{R_\mathrm{s} + \mathrm{j}\omega_\mathrm{m} L_\mathrm{s}} \frac{1-\underline{a}}{z-\underline{a}} \tag{3.25}$$

Using (3.20) and (3.24), the closed-loop behaviour of the current controller is obtained as

$$\underline{i}_\mathrm{s}(z) = \underline{G}(z)\underline{i}_\mathrm{s,ref}(z) - \underline{Y}_\mathrm{i}(z)\underline{u}_\mathrm{i}(z) \tag{3.26}$$

The closed-loop pulse-transfer functions for the reference following and the load-disturbance rejection can be rewritten in a more compact form as

$$\underline{G}(z) = \frac{\underline{b}_1 z + \underline{b}_0}{z^3 + \underline{a}_2 z^2 + \underline{a}_1 z + \underline{a}_0} \tag{3.27}$$

$$\underline{Y}_\mathrm{i}(z) = \frac{1-\underline{a}}{R_\mathrm{s} + \mathrm{j}\omega_\mathrm{m} L_\mathrm{s}} \frac{(z-1)(z+\underline{k}_2)}{z^3 + \underline{a}_2 z^2 + \underline{a}_1 z + \underline{a}_0} \tag{3.28}$$

where the coefficients can be obtained by comparing the results from (3.26) and (3.27) as

$$\underline{a}_0 = \underline{k}_2\underline{a} + \underline{b}(\underline{k}_\mathrm{i} - \underline{k}_1) \tag{3.29a}$$
$$\underline{a}_1 = \underline{a} + \underline{b}\,\underline{k}_1 - \underline{k}_2(1+\underline{a}) \tag{3.29b}$$
$$\underline{a}_2 = \underline{k}_2 - 1 - \underline{a} \tag{3.29c}$$
$$\underline{b}_0 = \underline{b}(\underline{k}_\mathrm{i} - \underline{k}_\mathrm{t}) \tag{3.29d}$$
$$\underline{b}_1 = \underline{b}\,\underline{k}_\mathrm{t} \tag{3.29e}$$

It should be noted that the coefficients $\underline{a}_0$, $\underline{a}_1$, $\underline{a}_2$, $\underline{b}_0$ and $\underline{b}_1$ are the actual coefficients of the closed-loop transfer function $\underline{G}(z)$ and $\underline{a}$, $\underline{b}$ are the actual parameters of the plant model. The intended coefficients are marked with the subscript $\star$ and the parameter estimates by a hat. Keeping these notations in mind, due to the effect of time delay, $\underline{a}_{0\star} = 0$ is selected. The gains of the current controller as a function of the coefficients of the closed-loop transfer function can be calculated as

$$\underline{k}_1 = \underline{k}_\mathrm{i} + \underline{k}_2\hat{\underline{a}}/\hat{\underline{b}} \tag{3.30a}$$
$$\underline{k}_2 = 1 + \underline{a}_{2\star} + \hat{\underline{a}} \tag{3.30b}$$
$$\underline{k}_\mathrm{i} = (1 + \underline{a}_{1\star} + \underline{a}_{2\star})/\hat{\underline{b}} \tag{3.30c}$$
$$\underline{k}_\mathrm{t} = \underline{b}_{1\star}/\hat{\underline{b}} \tag{3.30d}$$

The closed-loop poles and zero of (3.27) can be arbitrarily placed using the expressions of gains given in (3.30). The characteristic polynomial (denominator) of (3.27) can be expressed as

$$z(z^2 + \underline{a}_2 z + \underline{a}_1) = z(z - \underline{p}_1)(z - \underline{p}_2) \tag{3.31}$$

where $\underline{p}_1$ and $\underline{p}_2$ are the closed-loop poles. Hence, the coefficients $\underline{a}_1$ and $\underline{a}_2$ can be written in the form of poles $\underline{p}_1$ and $\underline{p}_2$ as $\underline{a}_1 = \underline{p}_1\underline{p}_2$ and $\underline{a}_2 = -\underline{p}_1 - \underline{p}_2$. Choosing the real values, the intended coefficients required in (3.30) become

$$\underline{a}_{1\star} = p_{1\star}^2, \quad \underline{a}_{2\star} = -2p_{1\star}, \quad \underline{b}_{1\star} = 1 - p_{1\star} \tag{3.32}$$

It can be seen from (3.30) that selecting the real coefficients, the gain expressions in (3.30) lead to the desired closed-loop pulse-transfer function of (3.17).

It is worth mentioning here that the gains in (3.30) depend on the rotor speed because of the discrete-time model parameters $\hat{\underline{a}}$ and $\hat{\underline{b}}$ as given in (2.21). The closed-loop pole is cancelled by the closed-loop zero in a similar manner as in the continuous-time case of (3.12). Furthermore, no extra parameters are required for the discrete-time design, rather the estimates of the same motor parameters ($\hat{R}_\mathrm{s}$, $\hat{L}_\mathrm{s}$) and the controller bandwidth α are needed.

3.4.2 Current Control of an IPMSM

The exact discrete-time model of an IPMSM given in Chapter 2 will be used as a starting point to design the controller for this motor. The model of an IPMSM is expressed as follows

$$\boldsymbol{i}_\mathrm{s}(k+1) = \boldsymbol{A}\boldsymbol{i}_\mathrm{s}(k) + \boldsymbol{B}\boldsymbol{u}_\mathrm{s}(k) + \boldsymbol{b}\psi_\mathrm{pm} \tag{3.33}$$

where the expressions for matrix elements can be found in Appendix A. If the matrix elements of the exact discrete-time model are computationally demanding, an approximate solution (series expansions) could be used instead. Some of the approximations are already presented in Chapter 2. More details about the current control using approximate motor models is presented in Section 3.5.

It should be noted that the complex space vectors used in the case of an SPMSM are now replaced with the real space vectors. The stator current vector is $\boldsymbol{i}_\mathrm{s} = [i_\mathrm{d},\ i_\mathrm{q}]^\mathrm{T}$, where i_d and i_q are the d- and q-components of the stator current vector and the superscript T is used to mark the matrix transpose.

The exact discrete-time model of an IPMSM using (3.33) can be written in a z-domain as

$$\begin{aligned} z\boldsymbol{i}_\mathrm{s}(z) &= \boldsymbol{A}\boldsymbol{i}_\mathrm{s}(z) + \boldsymbol{B}\boldsymbol{u}_\mathrm{s}(z) + \boldsymbol{b}\psi_\mathrm{pm} \\ \boldsymbol{i}_\mathrm{s}(z) &= (z\boldsymbol{I} - \boldsymbol{A})^{-1}\boldsymbol{B}\boldsymbol{u}_\mathrm{s}(z) + (z\boldsymbol{I} - \boldsymbol{A})^{-1}\boldsymbol{b}\psi_\mathrm{pm} \end{aligned} \tag{3.34}$$

The stator voltage expressed in terms of the reference voltage is

$$\boldsymbol{u}_{\mathrm{s}}(z) = \frac{\boldsymbol{u}'_{\mathrm{s,ref}}(z)}{z} \tag{3.35}$$

Using (3.34) and (3.35), the stator current in terms of pulse transfer functions can be expressed as

$$\boldsymbol{i}_{\mathrm{s}}(z) = \boldsymbol{Y}(z)\boldsymbol{u}'_{\mathrm{s,ref}}(z) - \boldsymbol{Y}_{\mathrm{i}}(z)\boldsymbol{u}_{\mathrm{i}}(z) \tag{3.36}$$

where

$$\boldsymbol{Y}(z) = z^{-1}(z\boldsymbol{I} - \boldsymbol{A})^{-1}\boldsymbol{B} \tag{3.37}$$

is a 2×2 reference following pulse-transfer-function matrix. The computational time delay is taken into account in a similar manner as in the case of an SPMSM

The induced voltage due to the PM flux and the corresponding pulse-transfer-function matrix are defined as follows

$$\boldsymbol{u}_{\mathrm{i}}(z) = [0, \omega_{\mathrm{m}}\psi_{\mathrm{pm}}]^{\mathrm{T}} \tag{3.38a}$$

$$\boldsymbol{Y}_{\mathrm{i}}(z) = -(z\boldsymbol{I} - \boldsymbol{A})^{-1}[\boldsymbol{0}, \boldsymbol{b}/\omega_{\mathrm{m}}] \tag{3.38b}$$

where $\boldsymbol{0} = [0, 0]^{\mathrm{T}}$ is a null column vector. Similar to the case of an SPMSM, the induced voltage $\boldsymbol{u}_{\mathrm{i}}$ due to the PM flux can be seen as a disturbance input to the system. For the controller parameter calculations, following relation of the stator current can be used

$$\boldsymbol{i}_{\mathrm{s}}(z) = \boldsymbol{Y}(z)\boldsymbol{u}'_{\mathrm{s,ref}}(z) \tag{3.39}$$

where $\boldsymbol{u}'_{\mathrm{s,ref}}(z)$ is the reference voltage, which can be found in a similar way as for an SPMSM in (3.20). Only change is that the controller gains will now be 2×2 real matrices instead of complex scalars.

The pulse transfer function of the control law for an IPMSM is given as

$$\boldsymbol{u}'_{\mathrm{s,ref}}(z) = \boldsymbol{K}_{\mathrm{t}}\boldsymbol{i}_{\mathrm{s,ref}}(z) + \frac{\boldsymbol{K}_{\mathrm{i}}}{z-1}[\boldsymbol{i}_{\mathrm{s,ref}}(z) - \boldsymbol{i}_{\mathrm{s}}(z)] - \boldsymbol{K}_1\boldsymbol{i}_{\mathrm{s}}(z) - \frac{\boldsymbol{K}_2}{z}\boldsymbol{u}'_{\mathrm{s,ref}}(z) \tag{3.40}$$

where $\boldsymbol{K}_{\mathrm{t}}$, $\boldsymbol{K}_{\mathrm{i}}$, $\boldsymbol{K}_1$ and $\boldsymbol{K}_2$ are 2×2 gain matrices. The control law in (3.40) represents a 2DOF state-space controller with integral action shown in Figure 3.1. $\boldsymbol{K}_{\mathrm{t}}$ is the reference feedforward gain, $\boldsymbol{K}_{\mathrm{i}}$ is the integral gain and $\boldsymbol{K}_1$ and $\boldsymbol{K}_2$ are the state feedback gains.

Using (3.39) and (3.40), the closed-loop behaviour of the stator current can be obtained as

$$\boldsymbol{i}_{\mathrm{s}}(z) = \boldsymbol{G}(z)\boldsymbol{i}_{\mathrm{s,ref}}(z) \tag{3.41}$$

where $\boldsymbol{G}(z)$ is the closed-loop reference following pulse-transfer function given by

$$\boldsymbol{G}(z) = \frac{z\boldsymbol{B}_1 + \boldsymbol{B}_0}{z^3\boldsymbol{I} + z^2\boldsymbol{A}_2 + z\boldsymbol{A}_1 + \boldsymbol{A}_0} \tag{3.42}$$

where the coefficient matrices are

$$\boldsymbol{A}_0 = \boldsymbol{B}(\boldsymbol{K}_2\boldsymbol{B}^{-1}\boldsymbol{A} + \boldsymbol{K}_\mathrm{i} - \boldsymbol{K}_1) \tag{3.43a}$$
$$\boldsymbol{A}_1 = \boldsymbol{A} + \boldsymbol{B}[\boldsymbol{K}_1 - \boldsymbol{K}_2\boldsymbol{B}^{-1}(\boldsymbol{I} + \boldsymbol{A})] \tag{3.43b}$$
$$\boldsymbol{A}_2 = \boldsymbol{B}\boldsymbol{K}_2\boldsymbol{B}^{-1} - \boldsymbol{I} - \boldsymbol{A} \tag{3.43c}$$
$$\boldsymbol{B}_0 = \boldsymbol{B}(\boldsymbol{K}_\mathrm{i} - \boldsymbol{K}_\mathrm{t}) \tag{3.43d}$$
$$\boldsymbol{B}_1 = \boldsymbol{B}\boldsymbol{K}_\mathrm{t} \tag{3.43e}$$

It can be seen from (3.43) that the coefficient matrices for an IPMSM resemble the scalar coefficients of an SPMSM given in (3.29).

Cross-coupling between the d- and q-axis can be avoided only if the non-diagonal elements of $\boldsymbol{G}(z)$ are zero. In order to achieve the desired closed-loop dynamics of a first-order low pass filter (3.17), $\boldsymbol{G}(z)$ can be expressed as

$$\boldsymbol{G}(z) = \frac{b_{1\star}z + b_{0\star}}{z^3 + a_{2\star}z^2 + a_{1\star}z + a_{0\star}}\boldsymbol{I} \tag{3.44}$$

Choosing $a_{0\star} = 0$ due to the computational time delay as done for an SPMSM, the controller gains can be expressed as

$$\boldsymbol{K}_1 = \boldsymbol{K}_\mathrm{i} + \boldsymbol{K}_2\hat{\boldsymbol{B}}^{-1}\hat{\boldsymbol{A}} \tag{3.45a}$$
$$\boldsymbol{K}_2 = (1 + a_{2\star})\boldsymbol{I} + \hat{\boldsymbol{B}}^{-1}\hat{\boldsymbol{A}}\hat{\boldsymbol{B}} \tag{3.45b}$$
$$\boldsymbol{K}_\mathrm{i} = (1 + a_{1\star} + a_{2\star})\hat{\boldsymbol{B}}^{-1} \tag{3.45c}$$
$$\boldsymbol{K}_\mathrm{t} = b_{1\star}\hat{\boldsymbol{B}}^{-1} \tag{3.45d}$$

The closed-loop poles and zero of (3.44) can be placed arbitrarily. Selecting coefficients $a_{1\star} = z_\mathrm{c}^2$, $a_{2\star} = -2z_\mathrm{c}$ and $b_{1\star} = 1 - z_\mathrm{c}$ result in the desired closed-loop pulse-transfer function (3.17). Where, z_c is the intended real pole of the system

$$z_\mathrm{c} = p_{1\star} = \mathrm{e}^{-\alpha T_\mathrm{s}} \tag{3.46}$$

It should be noted that the closed-loop pole is cancelled with a closed-loop zero in a similar way as for an SPMSM.

3.5 Approximate Discrete-Time Controllers

An analytical direct discrete-time pole-placement design method for the 2DOF state-space current controller with an integral action described in the last section will be used as a starting point for the gains calculation. Gains of the 2DOF state-space current controller will be calculated based on the continuous-time and approximate discrete-time (series expansion) models of an IPMSM and SyRM given in Chapter 2. All the design methods used for the gains calculation of the controller are as follows:

1. Emulation-based design
2. Approximate discrete-time design (series expansion)
   i) $\boldsymbol{F} = \boldsymbol{I}$
   ii) $\boldsymbol{F} = \boldsymbol{I} + \frac{\boldsymbol{A}_{\mathrm{c}} T_{\mathrm{s}}}{2}$

3.5.1 Emulation-based Design

Emulation-based design is the simplest way to obtain the discretized controller using the continuous-time design of the controller. The continuous-time gains given in (3.10) will be used as a starting point. The discrete-time implementation of an integral state can be done using the numerical approximations, i.e., the Euler and Tustin methods. The gains in the discrete-time domain are given as

$$\begin{aligned} \boldsymbol{K}_{\mathrm{t}} &= \alpha \hat{\boldsymbol{L}}_{\mathrm{s}}, \quad \boldsymbol{K}_{\mathrm{i}} = \alpha^2 T_{\mathrm{s}} \hat{\boldsymbol{L}}_{\mathrm{s}} \\ \boldsymbol{K}_1 &= 2\alpha \hat{\boldsymbol{L}}_{\mathrm{s}} - \hat{R}_{\mathrm{s}} \boldsymbol{I} - \omega_{\mathrm{m}} \boldsymbol{J} \hat{\boldsymbol{L}}_{\mathrm{s}}, \quad \boldsymbol{K}_2 = \boldsymbol{O} \end{aligned} \tag{3.47}$$

where

$$\boldsymbol{O} = \begin{bmatrix} 0 & 0 \\ 0 & 0 \end{bmatrix} \tag{3.48}$$

and the estimated motor parameters ($\hat{R}_{\mathrm{s}}$, $\hat{\boldsymbol{L}}_{\mathrm{s}}$) are used.

As described earlier, the ZOH of the stator voltage occurs naturally in the stator coordinates. In order to include the effect of the ZOH, an approximate solution in rotor coordinates was presented in [20]. The effect of the computational delay is already included in the coordinate transformation, shown in Figure 3.1. So, compensating the effect of time-delay caused by the ZOH with half a sampling period, the gains in (3.47) become

$$\begin{aligned} \boldsymbol{K}_{\mathrm{t}} &= \mathrm{e}^{(T_{\mathrm{s}}\omega_{\mathrm{m}}/2)\boldsymbol{J}} \alpha \hat{\boldsymbol{L}}_{\mathrm{s}}, \quad \boldsymbol{K}_{\mathrm{i}} = \mathrm{e}^{(T_{\mathrm{s}}\omega_{\mathrm{m}}/2)\boldsymbol{J}} \alpha^2 T_{\mathrm{s}} \hat{\boldsymbol{L}}_{\mathrm{s}} \\ \boldsymbol{K}_1 &= \mathrm{e}^{(T_{\mathrm{s}}\omega_{\mathrm{m}}/2)\boldsymbol{J}} \big(2\alpha \hat{\boldsymbol{L}}_{\mathrm{s}} - \hat{R}_{\mathrm{s}} \boldsymbol{I} - \omega_{\mathrm{m}} \boldsymbol{J} \hat{\boldsymbol{L}}_{\mathrm{s}}\big), \quad \boldsymbol{K}_2 = \boldsymbol{O} \end{aligned} \tag{3.49}$$

The gains of a synchronous-frame 2DOF PI controller for an IPMSM can be found in [21]. Compensation for the computational delay is also presented and implemented in the coordinate transformation. The integral state of the controller is implemented using the forward Euler approximation. The emulation-based design with the Tustin approximation is suitable when the sampling instant is small, making the ratio between the sampling and the fundamental frequency greater than 10 [34].

The forward Euler approximation gives satisfactory results when the frequency ratio is about twenty [5]. If the frequency ratio is less than twenty, the actual closed-loop system deviates significantly from the continuous-time design. Due to

discretization errors, cross-coupling exists between the d- and q-components of the stator current which leads to oscillations in the current waveform or even instability [5]. The cross-coupling between the axes increase with the increase in fundamental frequency.

3.5.2 Series Approximations of the Exact Discrete-Time Model

Series approximations of the exact discrete-time model for an IPMSM are given in Chapter 2. Using those results, the system matrices are found considering the stator flux as a state variable. The results can then be extended for the case with the stator current as a state variable.

Case 1: $\boldsymbol{F} = \boldsymbol{I}$

Using this approximation, we get the following results

$$\boldsymbol{A}_\mathrm{d} = \boldsymbol{I} + T_\mathrm{s}\boldsymbol{A}_\mathrm{c}, \qquad \boldsymbol{B}_\mathrm{d} = T_\mathrm{s}\frac{\omega_\mathrm{m}T_\mathrm{s}/2}{\sin(\omega_\mathrm{m}T_\mathrm{s}/2)}\,\mathrm{e}^{-(\omega_\mathrm{m}T_\mathrm{s}/2)\boldsymbol{J}} \tag{3.50}$$

The results from the above equation corresponds to the forward Euler discretization of the continuous-time motor model. This kind of approximation is only feasible if the ratio between the sampling and fundamental frequencies is high. It can be seen from the formula of $\boldsymbol{B}_\mathrm{d}$ that the ZOH is assumed to be in rotor coordinates [20].

Case 2: $\boldsymbol{F} = \boldsymbol{I} + \frac{\boldsymbol{A}_\mathrm{c}T_\mathrm{s}}{2}$

Using this approximation, we get the following results

$$\boldsymbol{A}_\mathrm{d} = \boldsymbol{I} + T_\mathrm{s}\boldsymbol{A}_\mathrm{c}\Big(\boldsymbol{I} + \frac{\boldsymbol{A}_\mathrm{c}T_\mathrm{s}}{2}\Big), \quad \boldsymbol{B}_\mathrm{d} = T_\mathrm{s}\Big(\boldsymbol{I} + \frac{\boldsymbol{A}_\mathrm{c}T_\mathrm{s}}{2}\Big)\frac{\omega_\mathrm{m}T_\mathrm{s}/2}{\sin(\omega_\mathrm{m}T_\mathrm{s}/2)}\,\mathrm{e}^{-(\omega_\mathrm{m}T_\mathrm{s}/2)\boldsymbol{J}} \tag{3.51}$$

The results shown above are obtained using just the first two terms from the Taylor series expansion of $\boldsymbol{F}$. If we increase the number of terms in the series expansion, the results will become very close to the exact model. If the frequency ratio is chosen to be higher than 10, the approximation given in (3.51) gives very good results, comparable to the exact discrete-time model.

3.6 Robustness

The system of equations used to study the robustness of a linear control system described in the last few sections are as follows

$$\boldsymbol{i}_\mathrm{s}(k+1) = \boldsymbol{A}\boldsymbol{i}_\mathrm{s}(k) + \boldsymbol{B}\boldsymbol{u}_\mathrm{s}(k) + \boldsymbol{b}\psi_\mathrm{pm} \tag{3.52a}$$

$$\boldsymbol{u}_\mathrm{s}(k+1) = \boldsymbol{K}_\mathrm{t}\boldsymbol{i}_\mathrm{s,ref}(k) + \boldsymbol{K}_\mathrm{i}\boldsymbol{x}_\mathrm{i}(k) - \boldsymbol{K}_1\boldsymbol{i}_\mathrm{s}(k) - \boldsymbol{K}_2\boldsymbol{u}_\mathrm{s}(k) \tag{3.52b}$$

$$\boldsymbol{x}_\mathrm{i}(k+1) = \boldsymbol{x}_\mathrm{i}(k) + \boldsymbol{i}_\mathrm{s,ref}(k) - \boldsymbol{i}_\mathrm{s}(k) \tag{3.52c}$$

The first equation represents the machine model and the next two give the controller design. The closed-loop state-space representation of the current control is formulated as follows

$$\begin{bmatrix} \boldsymbol{i}_\mathrm{s}(k+1) \\ \boldsymbol{u}_\mathrm{s}(k+1) \\ \boldsymbol{x}_\mathrm{i}(k+1) \end{bmatrix} = \underbrace{\begin{bmatrix} \boldsymbol{A} & \boldsymbol{B} & \boldsymbol{O} \\ -\boldsymbol{K}_1 & -\boldsymbol{K}_2 & \boldsymbol{K}_\mathrm{i} \\ -\boldsymbol{I} & \boldsymbol{O} & \boldsymbol{I} \end{bmatrix}}_{\boldsymbol{\Phi}} \begin{bmatrix} \boldsymbol{i}_\mathrm{s}(k) \\ \boldsymbol{u}_\mathrm{s}(k) \\ \boldsymbol{x}_\mathrm{i}(k) \end{bmatrix} + \begin{bmatrix} \boldsymbol{O} \\ \boldsymbol{K}_\mathrm{t} \\ \boldsymbol{I} \end{bmatrix} \boldsymbol{i}_{\mathrm{s,ref}}(k) + \begin{bmatrix} \boldsymbol{b} \\ \boldsymbol{O} \\ \boldsymbol{O} \end{bmatrix} \psi_\mathrm{pm} \tag{3.53}$$

The eigenvalues of the system matrix $\boldsymbol{\Phi}$ will give the stable region of the complete system. If the eigenvalues of the system matrix are inside the unit circle, it will represent a stable system otherwise unstable.

It should be noted that the gains of the controller are considered constant (based on the rated motor parameters) in this analysis. The variation of parameters are introduced in the machine model (matrices $\boldsymbol{A}$ and $\boldsymbol{B}$). Similar results can be obtained by changing the controller parameters to be variable and considering the machine model to be constant.

In an actual system, the variation in parameters especially the inductances is significant due to the phenomenon of magnetic saturation. The variation in inductances can be very high, even during one sampling period. This variation causes an additional bandwidth limitations.

Chapter 4

Results

The results in this thesis are divided into three main parts. First the analytical approach will be used to study the robustness of different controllers given in Chapter 3. Then the controllers will be tested using simulations and at the end, the results of experiments are presented. The experiments are performed on a transverse-laminated 6.7-kW four-pole SyRM whose rated values are given in Table 4.1. Four different current control designs have been evaluated:

Case 1: Emulation-based design

Case 2: Series approximation of the exact discrete-time model with $\boldsymbol{F} = \boldsymbol{I}$

Case 3: Series approximation of the exact discrete-time model with $\boldsymbol{F} = \boldsymbol{I} + \frac{\boldsymbol{A}_{\mathrm{c}} T_{\mathrm{s}}}{2}$

Case 4: The exact discrete-time model

Table 4.1: Ratings of the SyRM used in simulations and experiments.

Rated power	P_{N}	6.7 kW
Rated voltage (rms L-L)	U_{N}	370 V
Rated current (rms)	I_{N}	15.5 A
Rated frequency	f_{N}	105.8 Hz
Rated torque	T_{N}	20.1 Nm
Rated speed	ω_{m}	3175 r/min
Pole pairs	p	2

4.1 Robustness Analysis

The robustness of the four current control designs (Case 1 – 4) against parameter errors is analyzed by calculating the eigenvalues of the system matrix given in (3.53). Stability maps are produced for two different sampling frequencies of 1 and 2 kHz. Different control designs were presented in Chapter 3, but due to brevity only selected control designs are presented here. Robustness of the controller against the variation in L_d, L_q and R_s is studied separately. It should be noted that the machine model (3.52a) is always considered to be based on the exact discrete-time model in this analysis.

4.1.1 Variation in L_d

First the results are presented with the variation in the d-axis inductance. The controller gains are calculated using the parameter estimates $\hat{L}_\mathrm{d} = 2.0$ p.u., $\hat{L}_\mathrm{q} = 0.3$ p.u., and $\hat{R}_\mathrm{s} = 0.04$ p.u.. The actual inductance L_d is varied in a range from 0 to $2.5\hat{L}_\mathrm{d}$ while, the other actual parameters are kept constant (equal to their estimates). The desired bandwidth α is varied in a range from 0 to $2\pi{\cdot}500$ rad/s.

Results for two different rotor speeds are given here. Figure 4.1 shows the stability maps as a function of the desired bandwidth α and the ratio $L_\mathrm{d}/\hat{L}_\mathrm{d}$. It can be seen from Figure 4.1 that at a sampling frequency of 1 kHz and $\omega_\mathrm{m} = 0$ rad/s, the results from Case 2, 3 and 4 are overlapping. It means that at this sampling frequency and rotor speed, there is not much difference in the stability of the overall system for different cases. From Figure 4.1 it can be seen that as the sampling frequency increases, the region of stability increases for all the cases as expected. Similarly at a rotor speed of $\omega_\mathrm{m} = 2\pi \cdot 200$ rad/s, the results for two different sampling frequencies of 1 and 2 kHz are given in Figure 4.2. At this high speed, the emulation-based design is unstable for a sampling frequency of 1 kHz. One reason behind this instability is the small value of the frequency ratio. The exact model has the largest stability area at 1 kHz. It can be seen from Figure 4.2(b) that the stability regions for Case 3 and 4 overlaps at a sampling frequency of 2 kHz. It was expected as the approximation (Case 3) becomes nearly equal to that of the exact model at high frequency ratios.

4.1.2 Variation in L_q

Similar kind of variation was introduced in L_q keeping all the other parameters fixed (equal to their estimates), the results are shown in Figure 4.3. Comparing Figure 4.2 and Figure 4.3, it can be seen that the results are almost similar which concludes that the effect of variation in L_q on the system is similar to that of L_d. For this reason, only some of the results for the variation in L_q are shown here.

4.1.3 Variation in R_s

Variation in the actual value of stator resistance R_s is introduced in a similar way as in the case of L_d and L_q. The actual value of R_s is varied from 0 to $2.5\hat{R}_s$ while, the other parameters are kept constant (equal to their estimates). The variation in R_s is tested at two different rotor speeds ($\omega_m = 0$ and $\omega_m = 2\pi \cdot 200$ rad/s) and a sampling frequency of 2 kHz. It can be seen from Figure 4.4(a) that the stable region for Case 1 remains same throughout the parameter range. As expected, the current control is insensitive to the variation in the model resistance. The stable region for the other cases spans over the whole range as shown in Figure 4.4(a). Similarly at a speed of $\omega_m = 2\pi \cdot 200$ rad/s, the results are almost similar to Figure 4.4(a), making the current control independent of the variation in the stator resistance.

Stability maps were also developed for a sampling frequency of 1 kHz and rotor speeds of $\omega_m = 0$ and $2\pi \cdot 200$ rad/s, the results also show that the current control is independent of the variation in the stator resistance. Case 1 was unstable at a sampling frequency of 1 kHz and $\omega_m = 2\pi \cdot 200$ rad/s due to the low sampling frequency; not the variation in R_s.

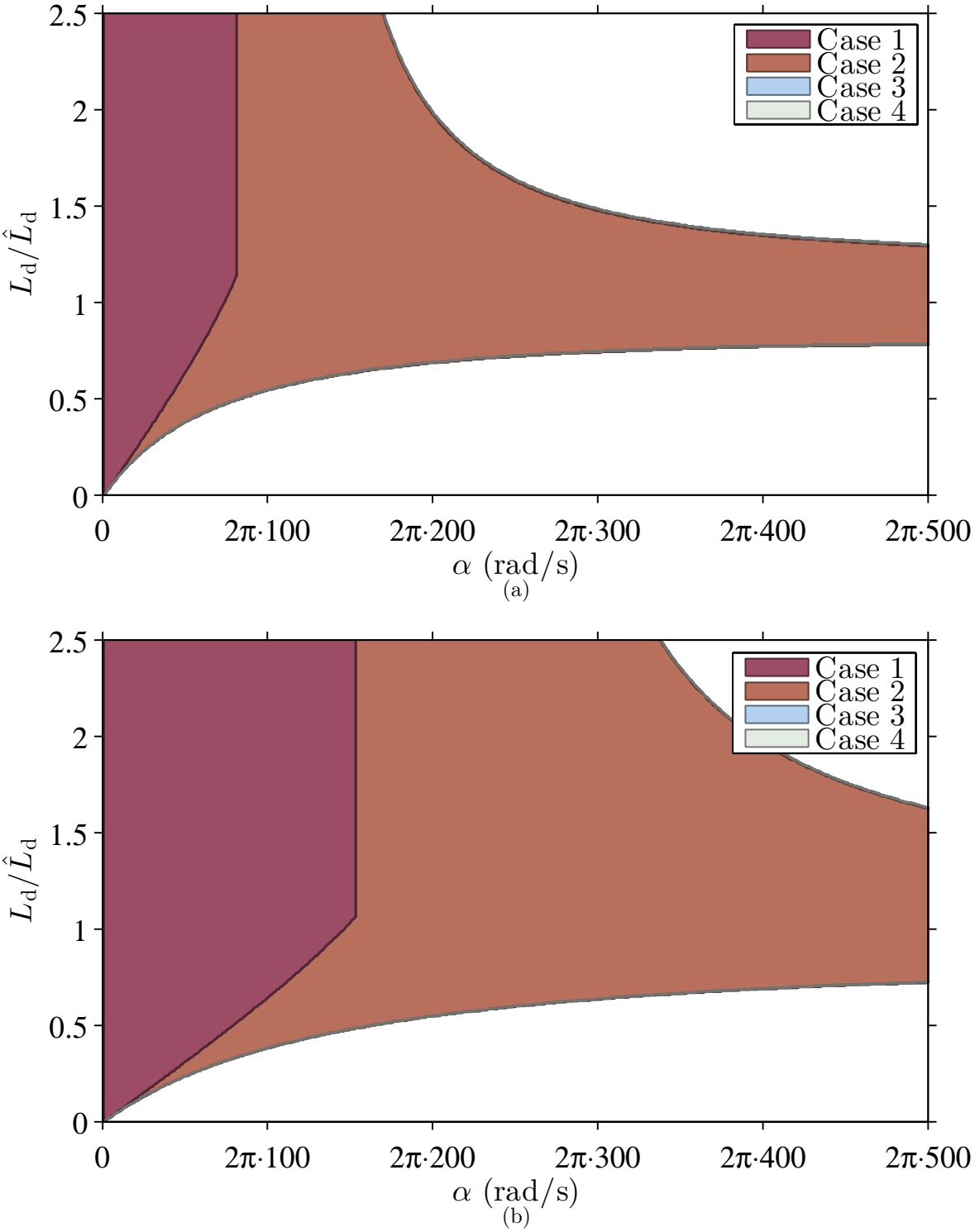

Figure 4.1: Stability maps for all 4 cases at $\omega_m = 0$ rad/s and $\alpha = 2\pi \cdot 100$ rad/s (a) $f_s = 1$ kHz (b) $f_s = 2$ kHz.

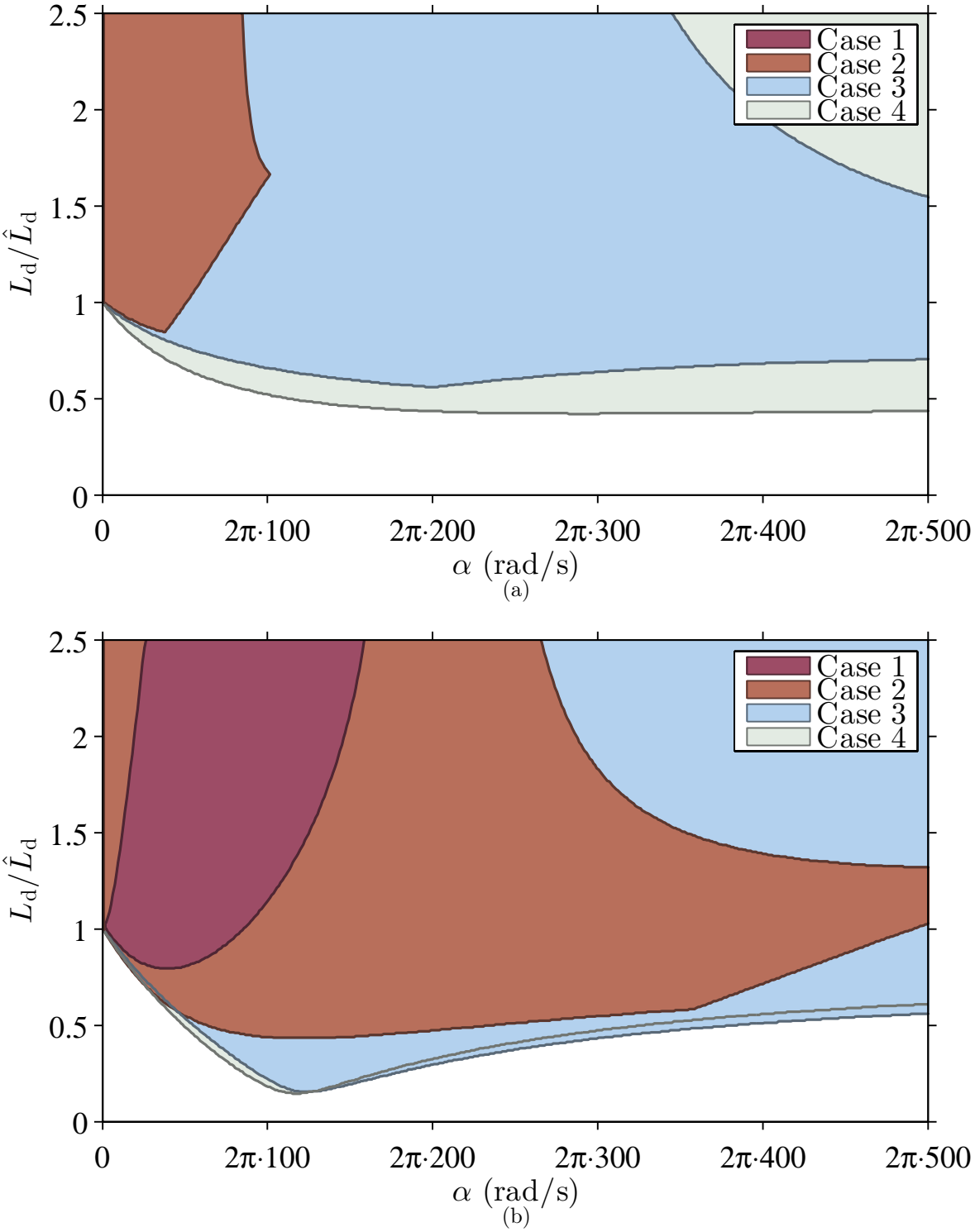

Figure 4.2: Stability maps for all 4 cases at $\omega_m = 2\pi \cdot 200$ rad/s and $\alpha = 2\pi \cdot 100$ rad/s (a) $f_s = 1$ kHz (b) $f_s = 2$ kHz.

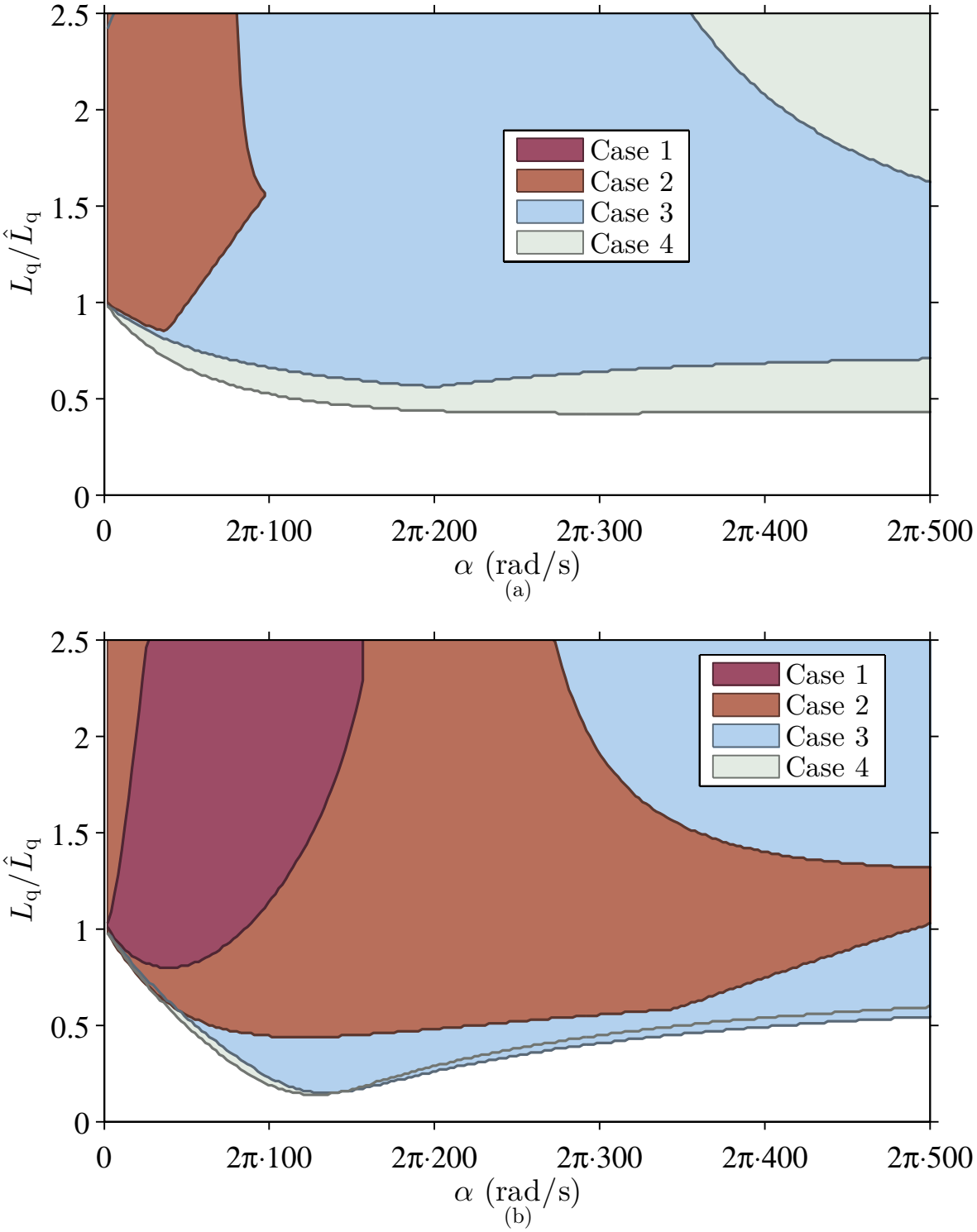

Figure 4.3: Stability maps for all 4 cases with variation in L_q at $\omega_m = 2\pi \cdot 200$ rad/s and $\alpha = 2\pi \cdot 100$ rad/s (a) $f_s = 1$ kHz (b) $f_s = 2$ kHz.

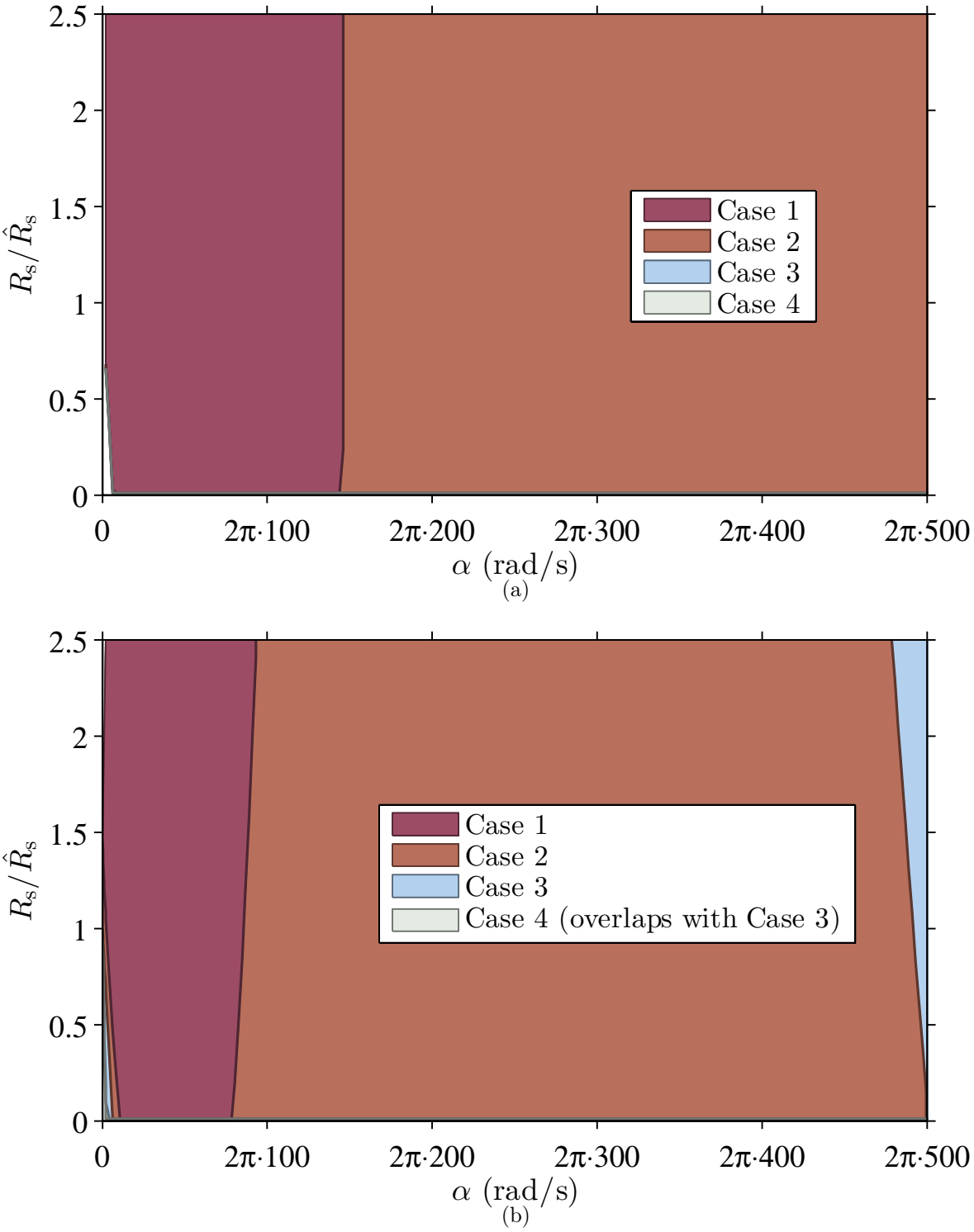

Figure 4.4: Stability maps for all 4 cases with variation in R_s at $f_s = 2$ kHz and $\alpha = 2\pi \cdot 100$ rad/s (a) $\omega_m = 0$ rad/s (b) $\omega_m = 2\pi \cdot 200$ rad/s.

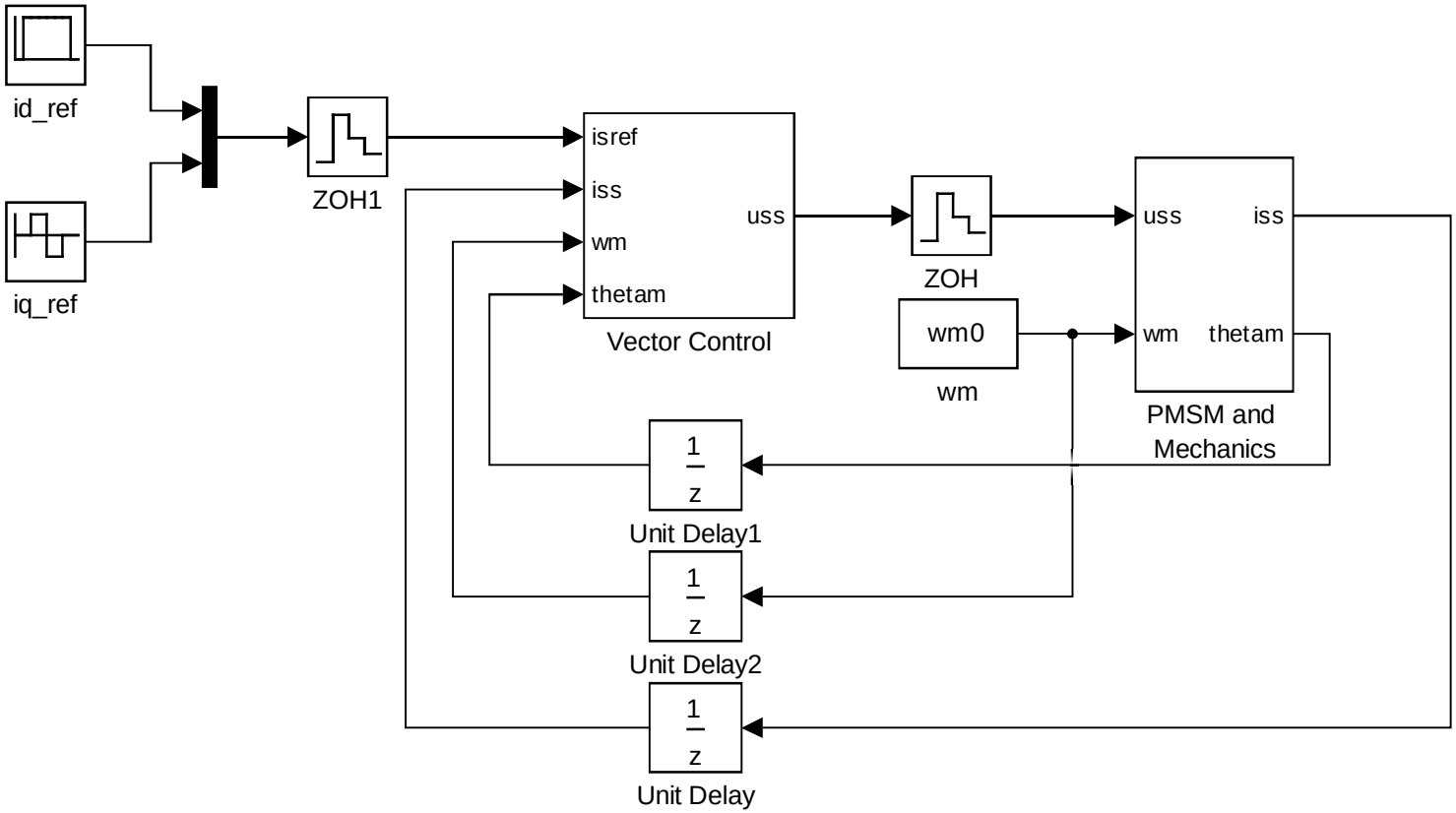

Figure 4.5: Simulation model of a SyRM drive.

4.2 Simulations

Simulations are performed on a 6.7-kW SyRM and the corresponding simulation model is shown in Figure 4.5. The "PMSM and Mechanics subsystem" is based on the continuous-time model of the SyRM and the "Vector Control" subsystem is based on different discrete-time controllers given in Chapter 3. All the input and output symbols are the same as used in this thesis, the input voltage and output current of the "PMSM and Mechanics" subsystem are in stator coordinates. Ratings and parameters of the SyRM are given in Table 4.1 and Table 4.2 respectively. It should be noted that the current shown in the results is the sampled current in synchronous coordinates, instead of the continuous-time current. Details about the inter-sampling current will be presented at the end of this analysis.

Simulations are performed at two different sampling frequencies of 1 and 2 kHz. Similarly, the current controllers for the SyRM are tested at two different speeds of $\omega_\mathrm{m} = 0$ and $\omega_\mathrm{m} = 2\pi \cdot 200$ rad/s, the bandwidth of the controller is kept constant at $\alpha = 2\pi \cdot 100$ rad/s. Three best cases are selected to compare the results: Case 2, Case 3 and Case 4. Case 1 which is the continuous-time design with the forward Euler discretization is unstable at a sampling frequency of 1 kHz. It works if we decrease the rotor speed to 0 rad/s and increase the sampling frequency to 2 kHz, but the overshoot is significant which deteriorates the performance of the controller as the rotor speed increases.

The comparison between Case 3 and Case 4 is presented at a sampling frequency of 1 kHz and a rotor speed $\omega_\mathrm{m} = 0$ rad/s. As mentioned earlier, the bandwidth of the current controller is kept constant at $\alpha = 2\pi \cdot 100$ rad/s. The results for these operating conditions are given in Figure 4.6. It can be seen from Figure 4.6 that the results for Case 3 and Case 4 are similar, but the difference seems to appear if the controller is simulated at a rotor speed of $\omega_\mathrm{m} = 2\pi \cdot 200$ rad/s. The results for these operating conditions are given in Figure 4.7. It can be seen from Figure 4.7(a) that the coupling between the d- and q-axis increases significantly as the rotor speed increases. Results for Case 4 as shown in Figure 4.7(b) remain the same as given in Figure 4.6.

Table 4.2: Parameters of the SyRM used in simulations and experiments.

Inductance on d-axis	L_d	45.6 mH
Inductance on q-axis	L_q	6.84 mH
Stator resistance	R_s	0.55 Ω
PM-flux	ψ_pm	0 Wb
Moment of inertia	J	0.015 kgm^2

Simulations were also performed for Case 2 at a sampling frequency of 1 and 2 kHz. The results for a rotor speed of 0 rad/s correspond to the ones given in Figure 4.6. At a rotor speed of $2\pi \cdot 200$ rad/s and a sampling frequency of 1 kHz, Case 2 is unstable. The results at a sampling frequency of 2 kHz are given in Figure 4.8. It can be seen from Figure 4.8(a) that the coupling between the d- and q-axis is significant, whereas in Figure 4.8(b) the coupling is reduced nearly to zero. The results from Figure 4.8(b) shows that Case 3 behaves like Case 4 if we increase the sampling frequency to 2 kHz.

Next the issue of inter-sampling current is discussed. The zoom-in of the continuous-time current at a sampling frequency of 1 kHz and a rotor speed of $2\pi \cdot 200$ rad/s is shown in Figure 4.9. It can be seen that the d- and q-axis currents vary significantly between the sampling instants and reach a certain value at the sampling instants. At the start of a step change in the q-axis current, there is a large overshoot which is not visible in a sampled current as shown in Figure 4.7. It is clearly visible from Figure 4.9(a) that there is a strong coupling between the d- and q-axis for Case 3, but Case 4 has no visible coupling, just an inter-sampling current. It can be seen that the sampled currents are not the average of the actual currents given in Figure 4.9. In order to solve this problem, a compensation method was presented in [18].

The idea behind the compensation method presented in [18] was to get the actual average current from the sampled current by introducing another component of the current called the average ripple current $\boldsymbol{i}_{\mathrm{s,ripple}}$ such that

$$\boldsymbol{i}_{\mathrm{s,total}} = \boldsymbol{i}_{\mathrm{s}} + \boldsymbol{i}_{\mathrm{s,ripple}} \tag{4.1}$$

where $\boldsymbol{i}_{\mathrm{s,total}}$ is the total value of the average current and $\boldsymbol{i}_{\mathrm{s}}$ is the average of sampled current. The additional ripple current $\boldsymbol{i}_{\mathrm{s,ripple}}$ will shift the continuous-time current such that the average of the actual continuous-time current is obtained between the two sampling instants, instead of peaks at the sampling instants. It is worth mentioning here that as the sampling frequency is increased, the inter-sampling current reduces and the value of $\boldsymbol{i}_{\mathrm{s,ripple}}$ approaches zero. For this reason, this compensation is not included in the simulations or experiments. But if the sampling frequency is reduced such that the frequency ratio is small (less than 10), the inter-sampling currents become significant and it is reasonable to compensate them in the controller model.

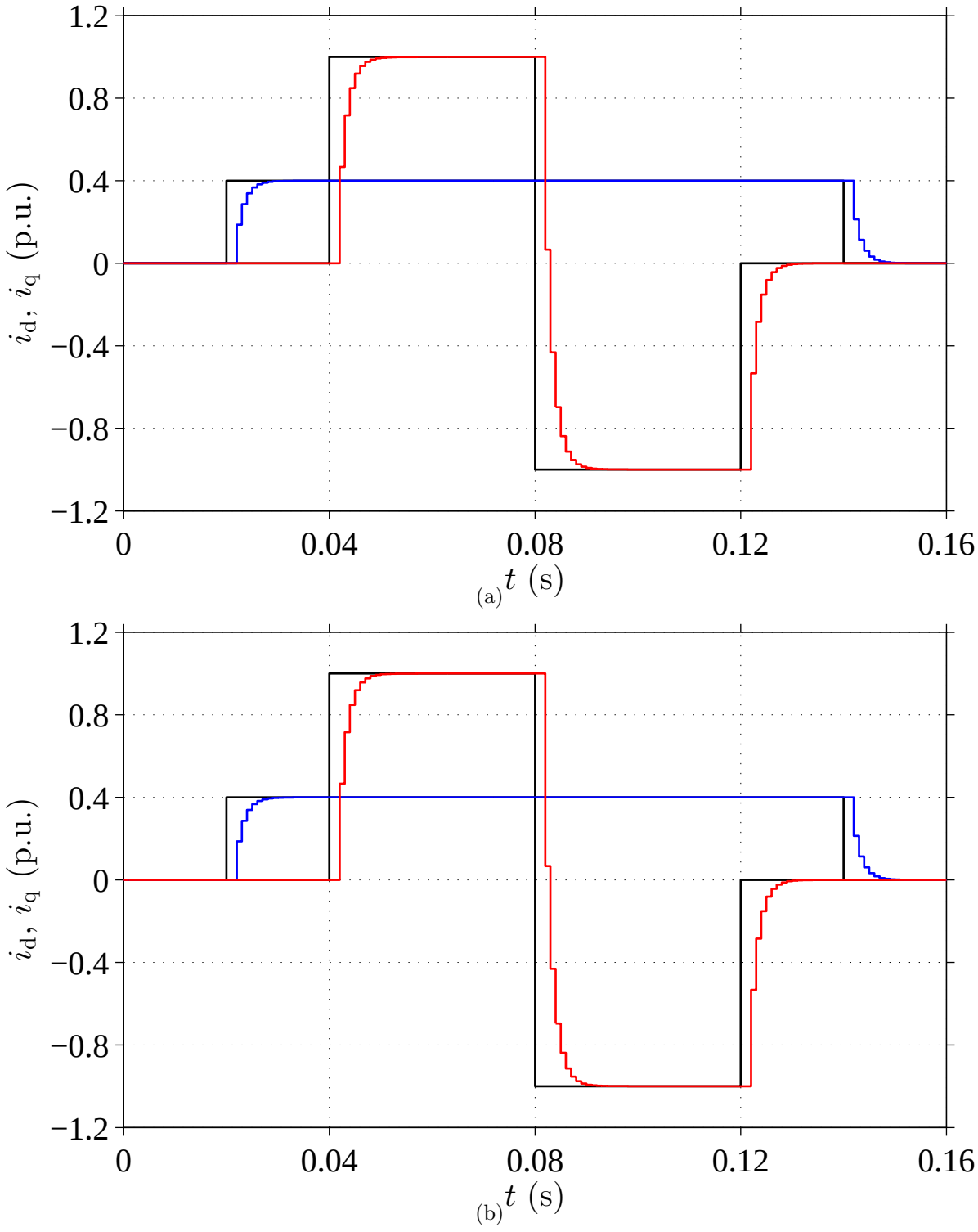

Figure 4.6: Simulation results showing sampled values of i_d (blue), i_q (red), and their references (black), when the speed is $\omega_\mathrm{m} = 0$ rad/s, the desired bandwidth is $\alpha = 2\pi \cdot 100$ rad/s, and the sampling frequency is 1 kHz: (a) Case 3: controller based on the approximate model with $\boldsymbol{F} = \boldsymbol{I} + (T_\mathrm{s}/2)\boldsymbol{A}$ (b) Case 4: controller based on the exact discrete-time model of the motor.

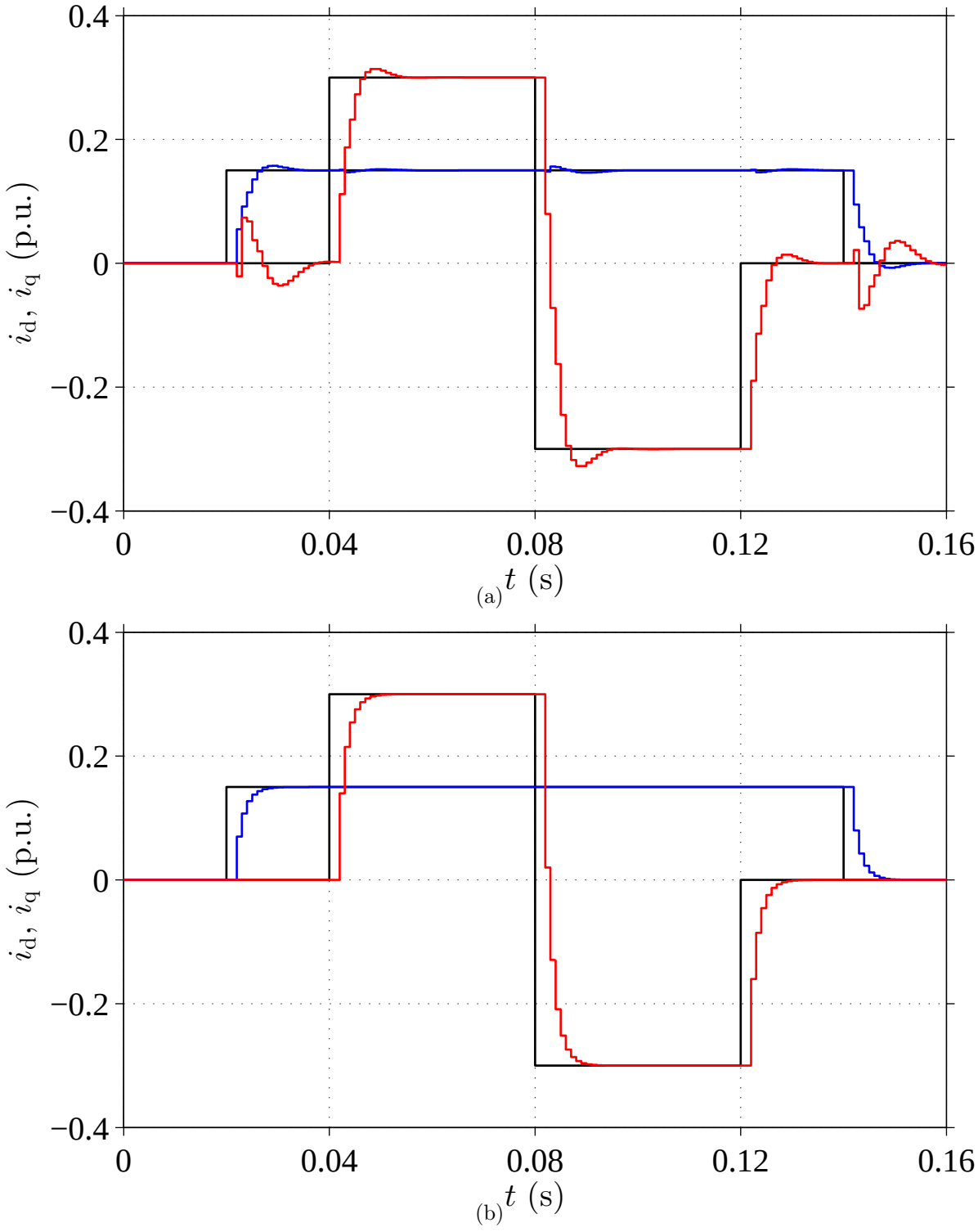

Figure 4.7: Simulation results showing sampled values of i_d (blue), i_q (red), and their references (black), when the speed is $\omega_\mathrm{m} = 2\pi \cdot 200$ rad/s, the desired bandwidth is $\alpha = 2\pi \cdot 100$ rad/s, and the sampling frequency is 1 kHz: (a) Case 3: controller based on the approximate model with $\boldsymbol{F} = \boldsymbol{I} + (T_\mathrm{s}/2)\boldsymbol{A}$ (b) Case 4: controller based on the exact discrete-time model of the motor.

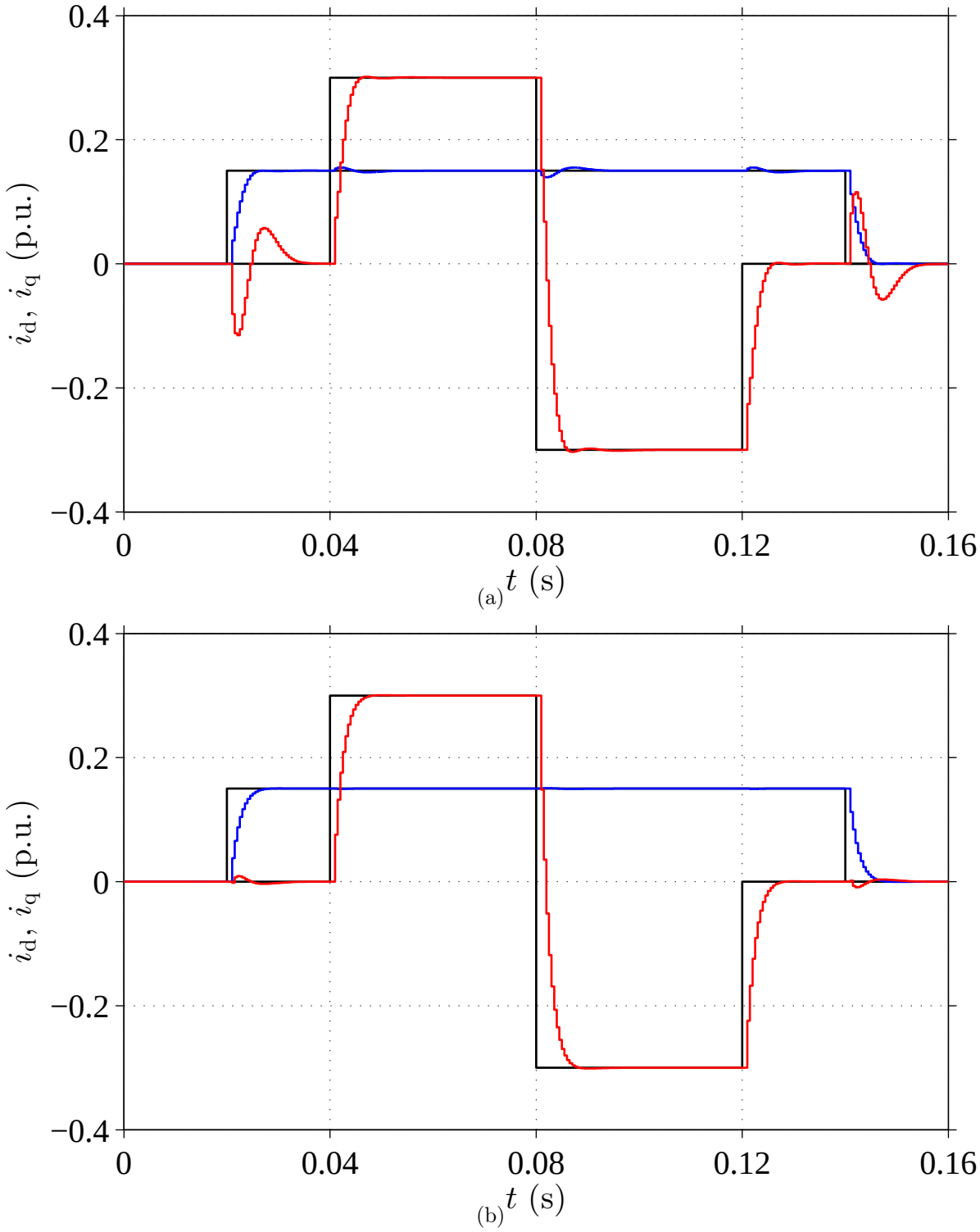

Figure 4.8: Simulation results showing sampled values of i_d (blue), i_q (red), and their references (black), when the speed is $\omega_\mathrm{m} = 2\pi \cdot 200$ rad/s, the desired bandwidth is $\alpha = 2\pi \cdot 100$ rad/s, and the sampling frequency is 2 kHz: (a) Case 2: controller based on the approximate model with $\boldsymbol{F} = \boldsymbol{I}$ (b) Case 3: controller based on the approximate model with $\boldsymbol{F} = \boldsymbol{I} + (T_\mathrm{s}/2)\boldsymbol{A}$.

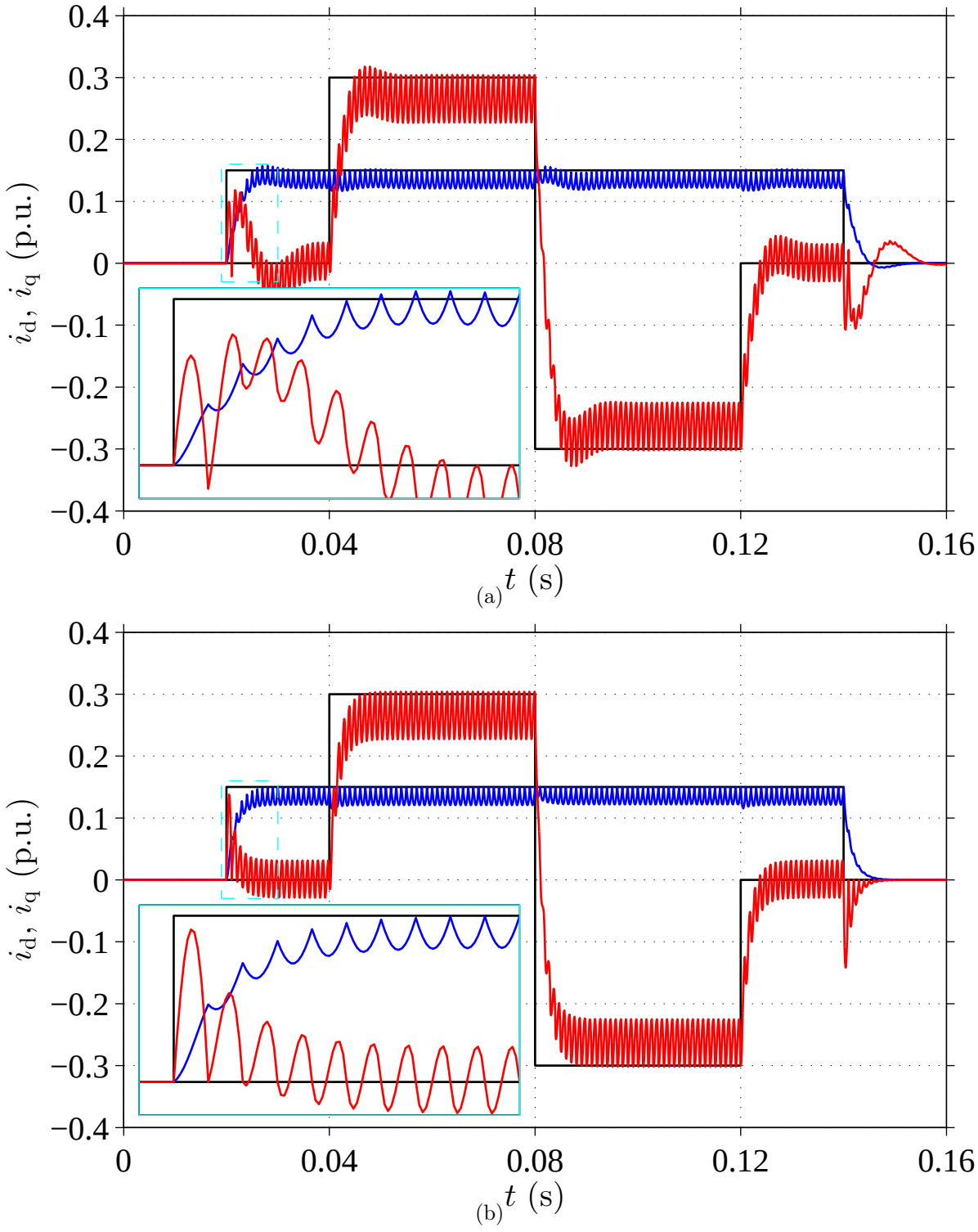

Figure 4.9: Simulation results showing the inter-sampled values of i_d (blue), i_q (red), and their references (black), when the speed is $\omega_\mathrm{m} = 2\pi \cdot 200$ rad/s, the desired bandwidth is $\alpha = 2\pi \cdot 100$ rad/s, and the sampling frequency is 1 kHz: (a) Case 3: controller based on the approximate model with $\boldsymbol{F} = \boldsymbol{I} + (T_\mathrm{s}/2)\boldsymbol{A}$ (b) Case 4: controller based on the exact discrete-time model of the motor.

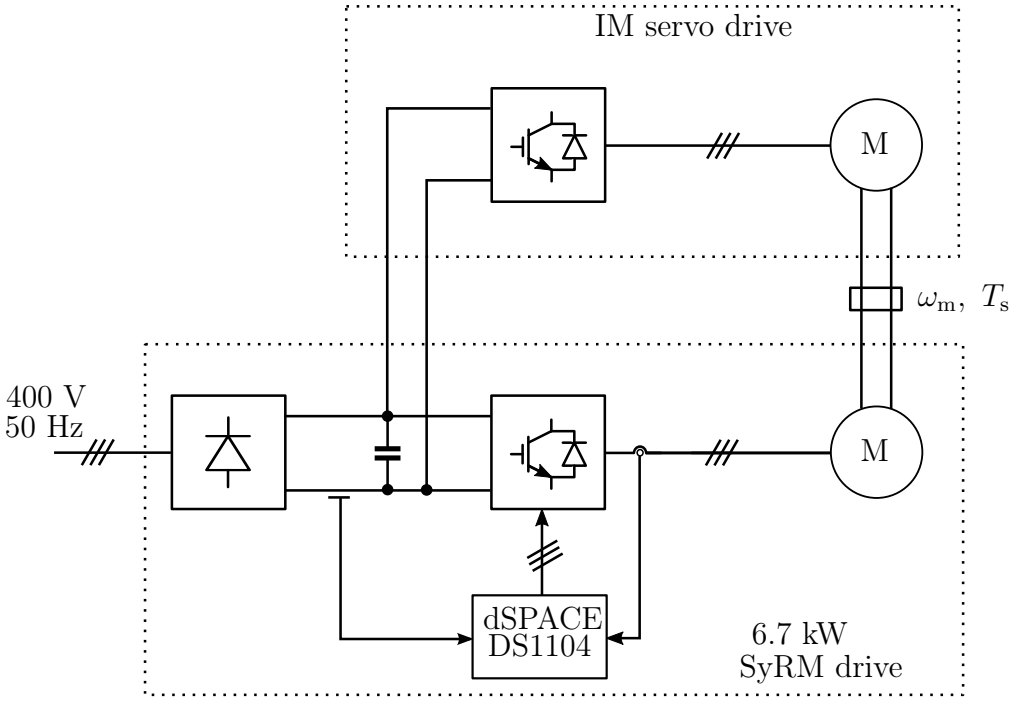

Figure 4.10: Block diagram of the experimental setup used in the laboratory test.

4.3 Experiments

4.3.1 Setup

The block diagram of the experimental setup is shown in Figure 4.10. Similar kind of setup with slight modifications was used in [35]. The control algorithms were implemented in a dSpace DS1104 PPC/DSP board. All the control algorithms are modelled in the Matlab/Simulink environment and then are compiled and loaded into the dSpace board.

The rated parameters and ratings of the SyRM used in experiments are given in Table 4.2 and Table 4.1. The SyRM is fed by a frequency converter controlled by the dSpace board, DS1104. It can be seen from Figure 4.10 that an IM servo drive is used as a load machine in a speed control mode. The rotor speed ω_m and rotor angle ϑ_m are measured using an incremental encoder. Different signals are measured for the control and monitoring purposes, the important ones are the stator current and the DC link voltage.

4.3.2 Magnetic Saturation

In order to achieve high torque density, SyRMs often run in extreme saturation conditions [36]. Due to the magnetic saturation, it is not reasonable to model the inductances as a constant. In order to achieve better control performance, the magnetic saturation has to be included in the model. The actual inductances L_d

Table 4.3: Fitted per-unit parameters

L_{du}	L_{qu}	α	β	γ	a	b	c	d
2.73	0.843	0.847	3.84	2.37	6.61	1.33	0.41	0

and L_{q} in the SyRM can be modelled as functions of the fluxes (or currents). The model proposed in [36] is as follows:

$$i_{\mathrm{d}}(\psi_{\mathrm{d}}, \psi_{\mathrm{q}}) = \frac{\psi_{\mathrm{d}}}{L_{\mathrm{du}}}\left[1 + (\alpha|\psi_{\mathrm{d}}|)^a + \frac{\gamma L_{\mathrm{du}}}{d+2}|\psi_{\mathrm{d}}|^c|\psi_{\mathrm{q}}|^{d+2}\right] \tag{4.2a}$$

$$i_{\mathrm{q}}(\psi_{\mathrm{d}}, \psi_{\mathrm{q}}) = \frac{\psi_{\mathrm{q}}}{L_{\mathrm{qu}}}\left[1 + (\beta|\psi_{\mathrm{q}}|)^b + \frac{\gamma L_{\mathrm{qu}}}{c+2}|\psi_{\mathrm{d}}|^{c+2}|\psi_{\mathrm{q}}|^d\right] \tag{4.2b}$$

where L_{du} and L_{qu} are the per-unit unsaturated inductances, and α, β, γ, a, b, c, and d are non-negative constants. It should be noted that this model inherently takes into account the cross-saturation between the d- and q-axis inductances.

The estimated inductances $\hat{L}_{\mathrm{d}}$ and $\hat{L}_{\mathrm{q}}$ were calculated in rotor coordinates using the measurement data. The measurements were carried out in steady state at a constant speed of $\omega_{\mathrm{m}} = 0.3$ p.u. The measurement range was $i_{\mathrm{d}} = 0.1 \ldots 0.7$ p.u. and $i_{\mathrm{q}} = -1.4 \ldots 1.4$ p.u. The inductance estimates were calculated as follows

$$\hat{L}_{\mathrm{d}} = \frac{u_{\mathrm{q}} - R_{\mathrm{s}} i_{\mathrm{q}}}{i_{\mathrm{d}}\omega_{\mathrm{m}}} \tag{4.3a}$$

$$\hat{L}_{\mathrm{q}} = \frac{u_{\mathrm{d}} - R_{\mathrm{s}} i_{\mathrm{d}}}{i_{\mathrm{q}}\omega_{\mathrm{m}}} \tag{4.3b}$$

The actual inductances L_{d} and L_{q} were calculated from the functions (4.2) using the actual values of the fluxes ψ_{d} and ψ_{q} in each operating point. The fitted per-unit parameters are given in Table 4.3. The measured inductance data and curves from the fitted functions are shown in Figure 4.11. It can be seen that the model proposed in [36] fits very well to the measured data. It is evident from Figure 4.11 that the cross-saturation is significant in the SyRM under study. If there was no cross-saturation, the curves in Figure 4.11 would overlap.

The effects of the differential inductance were not included for simplicity. In order to properly incorporate the effects of the differential inductance, following one-step predicted matrices should be used

$$\boldsymbol{A}(k) = \boldsymbol{C}(k+1)\boldsymbol{A}_{\mathrm{d}}(k)\boldsymbol{C}^{-1}(k) \tag{4.4a}$$

$$\boldsymbol{B}(k) = \boldsymbol{C}(k+1)\boldsymbol{B}_{\mathrm{d}}(k) \tag{4.4b}$$

The effects of the differential inductance were omitted and the following relations were used instead

$$\boldsymbol{A}(k) = \boldsymbol{C}(k)\boldsymbol{A}_{\mathrm{d}}(k)\boldsymbol{C}^{-1}(k) \tag{4.5a}$$

$$\boldsymbol{B}(k) = \boldsymbol{C}(k)\boldsymbol{B}_{\mathrm{d}}(k) \tag{4.5b}$$

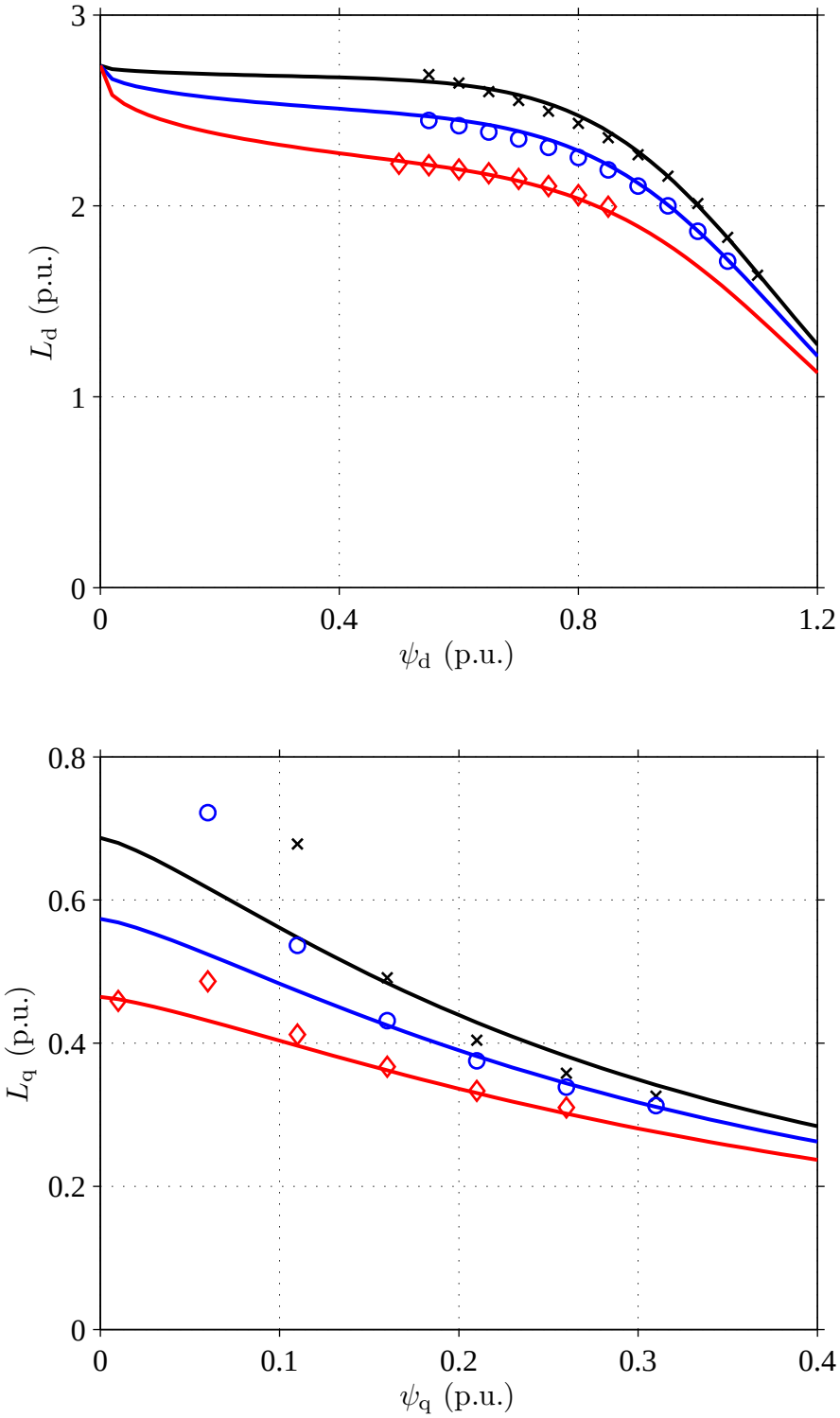

Figure 4.11: Results from curve fitting and experimental data: (a) L_d as a function of ψ_d for three different values of $\psi_q = \big[$0.1 p.u. (black line), 0.2 p.u. (blue line), 0.3 p.u. (red line)$\big]$; (b) L_q as a function of ψ_q for three different values of $\psi_d = \big[$0.6 p.u. (black line), 0.8 p.u. (blue line), 1.0 p.u. (red line)$\big]$ [36].

4.3.3 Results

Similar to the simulations, the experiments are also performed at two different speeds of 0 and $2\pi \cdot 200$ rad/s and two different sampling frequencies of 1 and 2 kHz. The controller bandwidth is kept constant at $\alpha = 2\pi \cdot 100$ rad/s. Figure 4.12 shows one of the experimental results at zero speed. The results from both the cases (Case 2 and 4) are similar, showing that the performance of all the control algorithms is almost identical at low speeds. The results in Figure 4.12 are in accordance with the stability maps of Figure 4.1. The results from Case 3 are also similar to that of Case 2 and 4 at $\omega_{\mathrm{m}} = 0$ rad/s. It can be seen that the controller gives desired performance except at the instants when there is a step change in the current references. This is due to the effect of magnetic saturation. It is expected that the oscillations and cross-coupling can be reduced by including the effects of differential inductance. The effects of magnetic saturation in IPMSMs and PM-assisted SyRMs are less severe in comparison with that of SyRM. Figure 4.13 shows the zero speed results at a sampling frequency of 1 kHz. It can be seen that the oscillations are grown due to large variations in L_{d} and L_{q} during one sampling period. The model used for the magnetic saturation does not give good results at this sampling frequency (large sampling time).

Figure 4.14 and Figure 4.15 show the results at a speed of $2\pi \cdot 200$ rad/s with two different frequencies of 1 and 2 kHz. It can be seen from Figure 4.14(a) that the controller does not give satisfactory results, but it is still stable or more appropriately marginally stable in accordance with the stability maps of Figure 4.2. Figure 4.14(b) shows the results for Case 4 at 1 kHz, the overshoot is very large (more than 50% in i_{q}) with high oscillations. Figure 4.15 shows very good results compared with Figure 4.14 as the sampling frequency increases to 2 kHz. The results from Case 2 are shown in Figure 4.15(a), the cross-coupling can be seen clearly and the oscillations are very large in comparison with Case 4 in Figure 4.15(b). The oscillations in Figure 4.15 can be reduced by including the effect of the differential inductance in the saturation. At a sampling frequency of 2 kHz, the results from Case 3 were similar to that of Case 4, in accordance with the stability maps of Figure 4.2.

It is worth mentioning here that the inverter voltage drops and the dead-time effects of the inverter switches are compensated inside the control algorithm. The output voltage of the current regulator is limited inside the control algorithm to about 0.9 p.u.

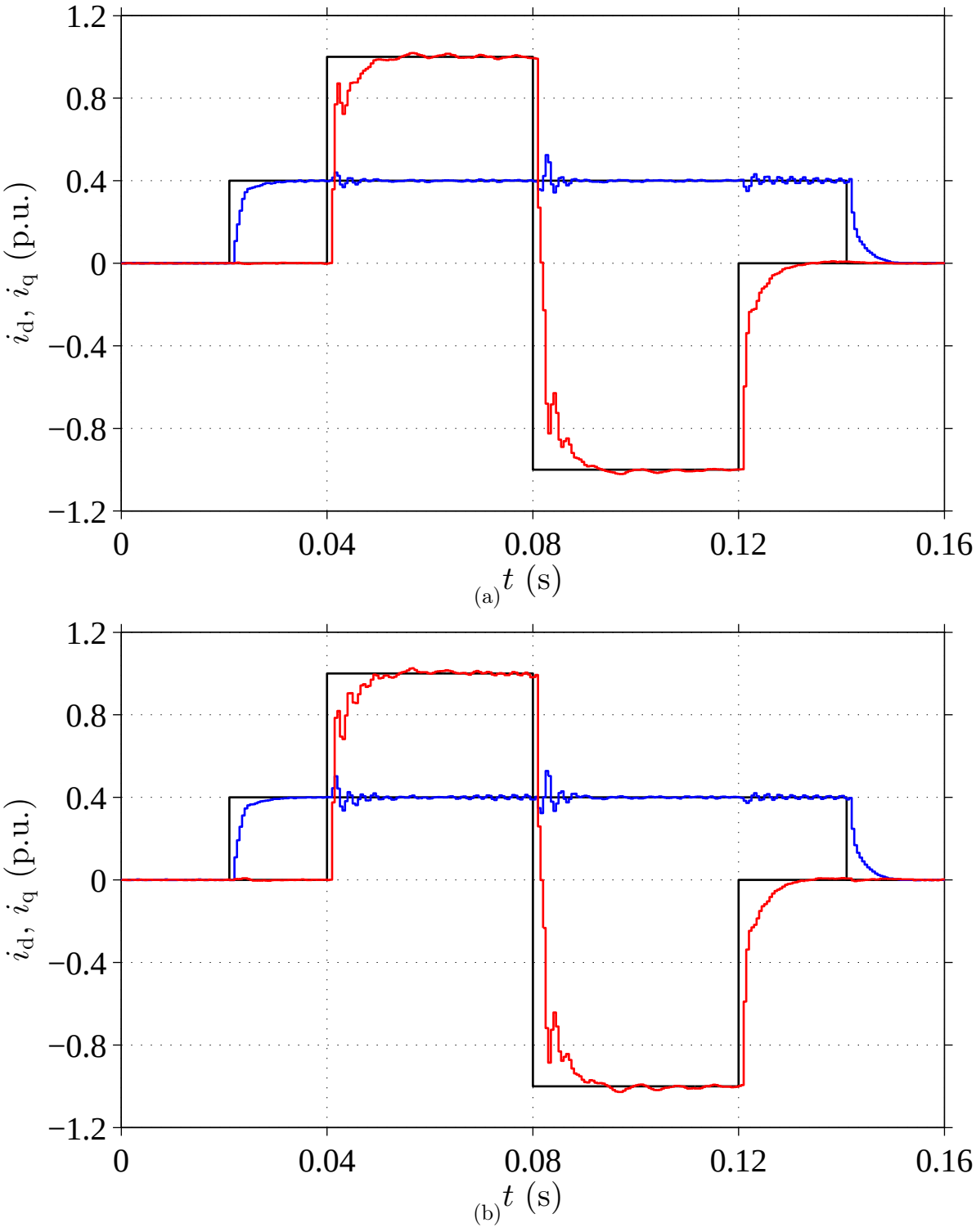

Figure 4.12: Experimental results showing sampled values of i_d (blue), i_q (red), and their references (black), when the speed is $\omega_\mathrm{m} = 0$ rad/s, the desired bandwidth is $\alpha = 2\pi \cdot 100$ rad/s, and the sampling frequency is 2 kHz: (a) Case 2: controller based on the approximate model with $\boldsymbol{F} = \boldsymbol{I}$ (b) Case 4: controller based on the exact discrete-time model of the motor.

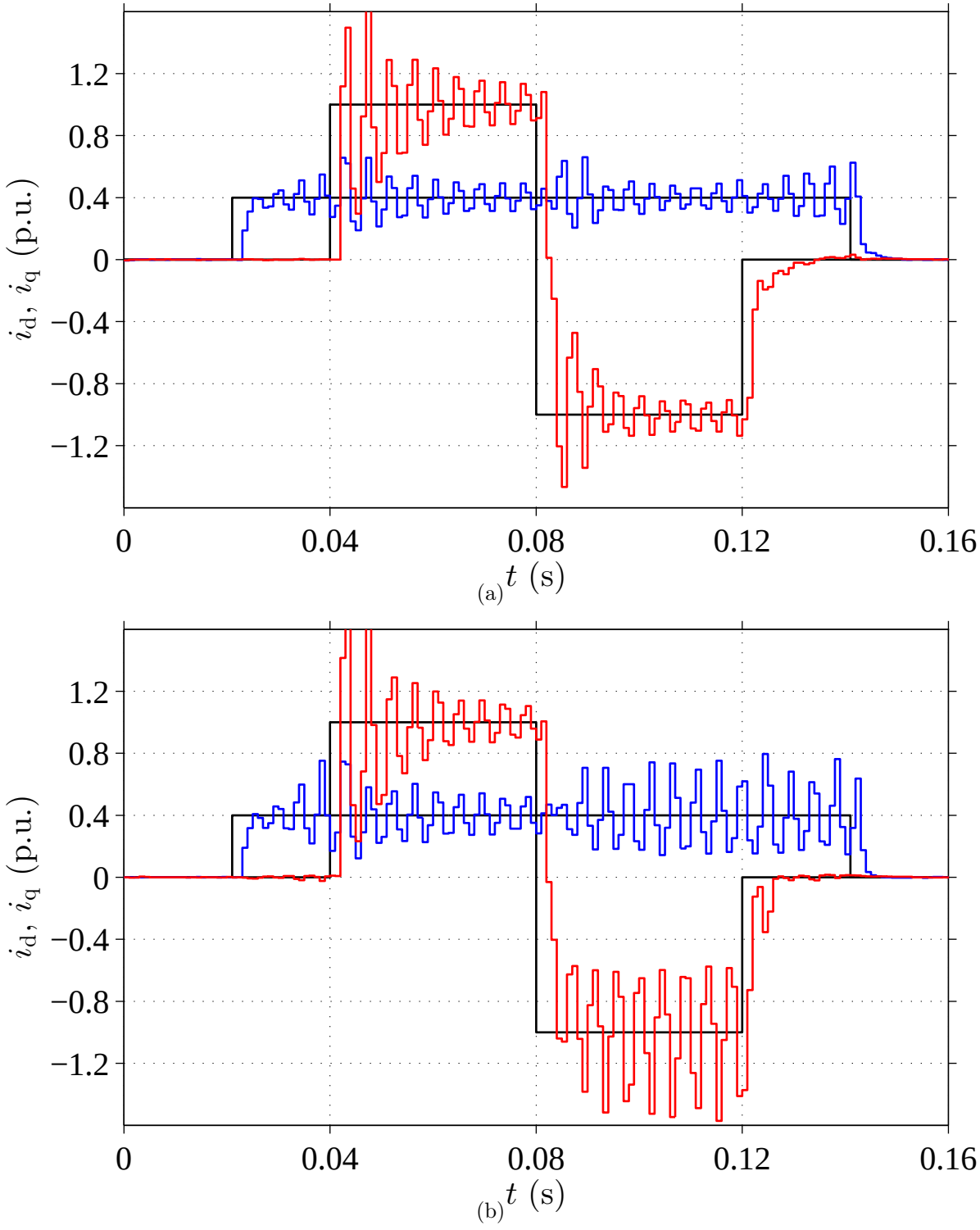

Figure 4.13: Experimental results showing sampled values of i_d (blue), i_q (red), and their references (black), when the speed is $\omega_\mathrm{m} = 0$ rad/s, the desired bandwidth is $\alpha = 2\pi \cdot 100$ rad/s, and the sampling frequency is 1 kHz: (a) Case 2: controller based on the approximate model with $\boldsymbol{F} = \boldsymbol{I}$ (b) Case 4: controller based on the exact discrete-time model of the motor.

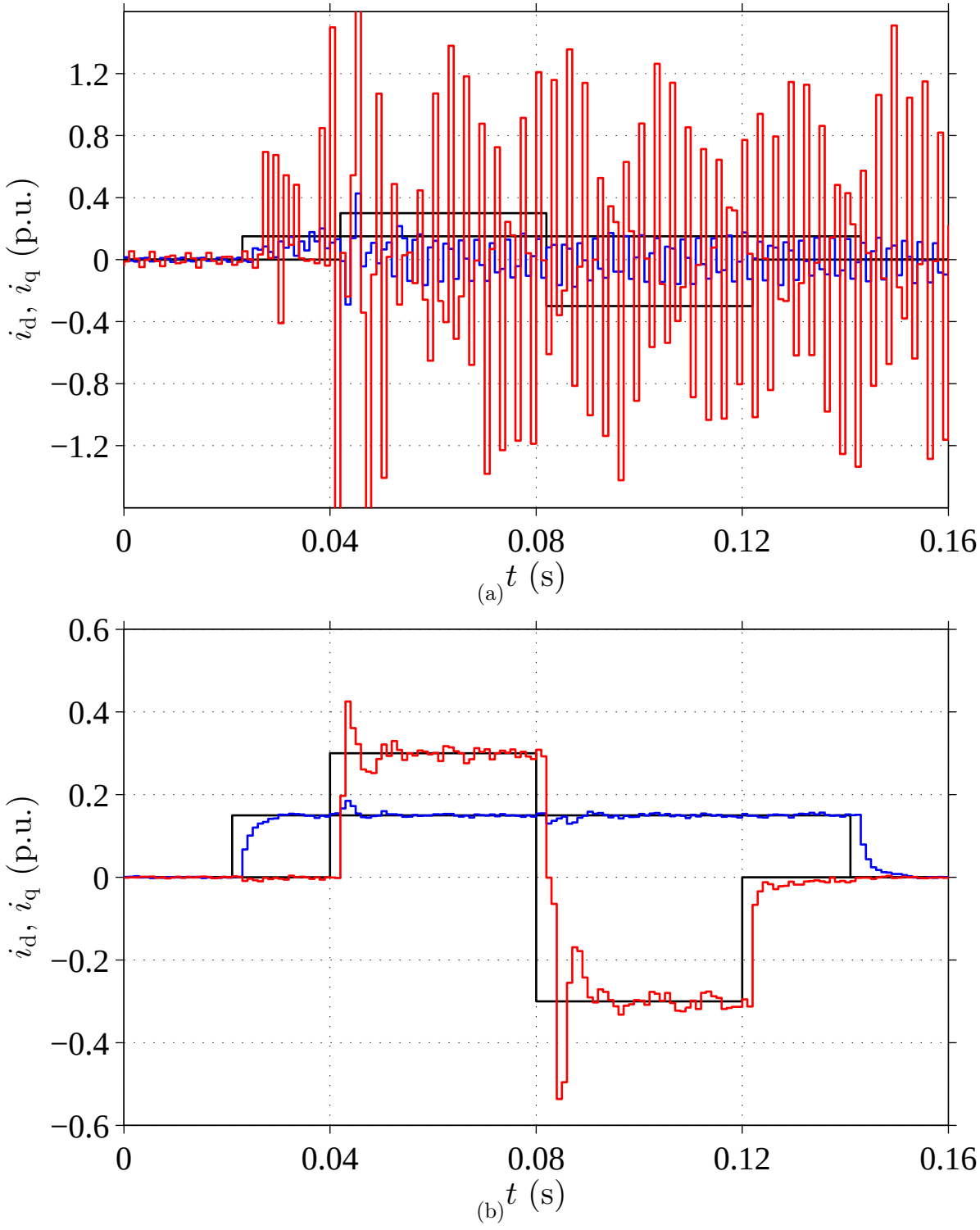

Figure 4.14: Experimental results showing sampled values of i_d (blue), i_q (red), and their references (black), when the speed is $\omega_\mathrm{m} = 2\pi \cdot 200$ rad/s, the desired bandwidth is $\alpha = 2\pi \cdot 100$ rad/s, and the sampling frequency is 1 kHz: (a) Case 2: controller based on the approximate model with $\boldsymbol{F} = \boldsymbol{I}$ (b) Case 4: controller based on the exact discrete-time model of the motor.

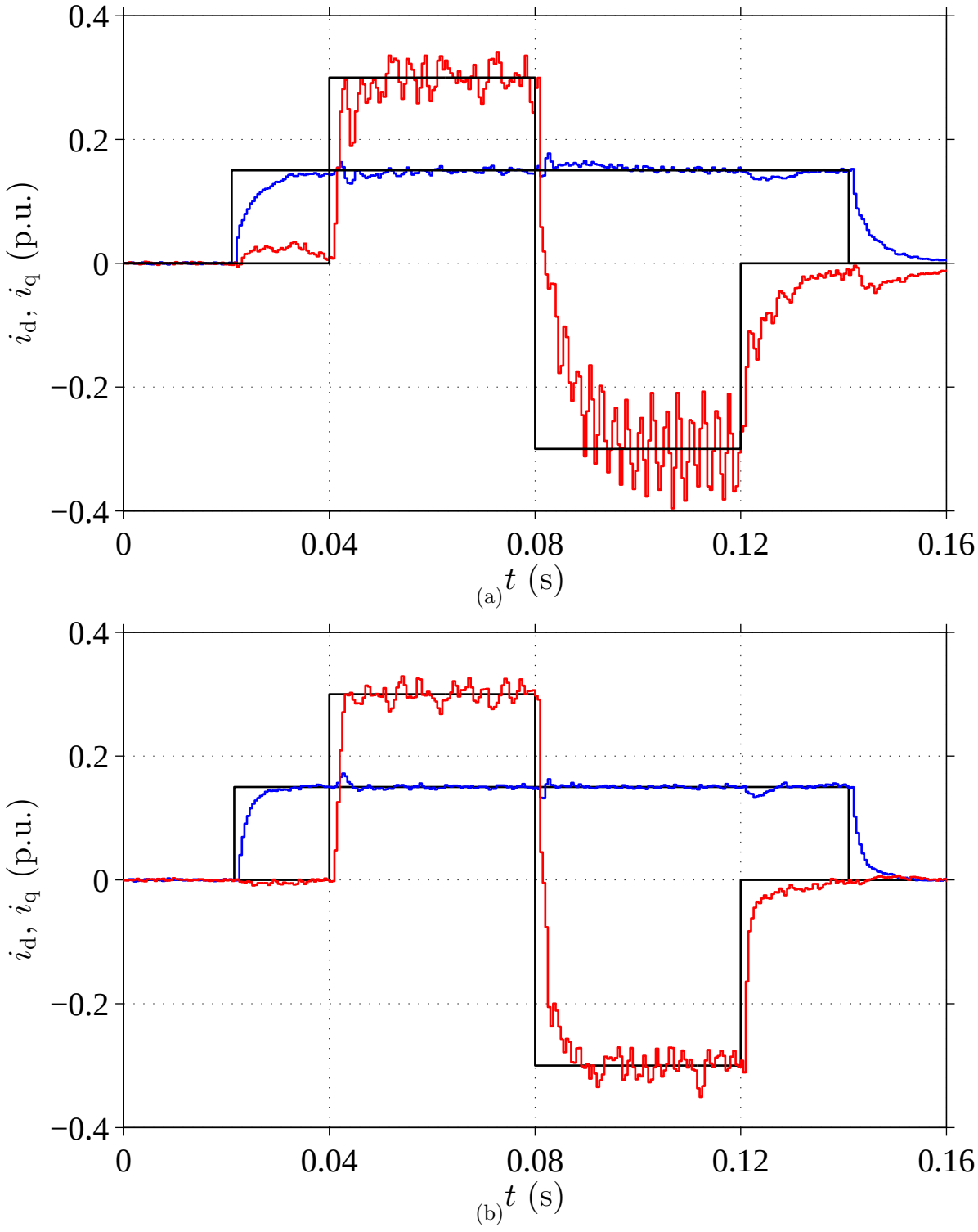

Figure 4.15: Experimental results showing sampled values of i_d (blue), i_q (red), and their references (black), when the speed is $\omega_\mathrm{m} = 2\pi \cdot 200$ rad/s, the desired bandwidth is $\alpha = 2\pi \cdot 100$ rad/s, and the sampling frequency is 2 kHz: (a) Case 2: controller based on the approximate model with $\boldsymbol{F} = \boldsymbol{I}$ (b) Case 4: controller based on the exact discrete-time model of the motor.

Chapter 5

Conclusions

In this thesis, the discrete-time models and current control of synchronous motors with a magnetically anisotropic rotor structure, such as IPMSMs and SyRMs were studied. The exact discrete-time model of the SyRM and IPMSM was studied with the ZOH assumed in the stator coordinates, where it occurs naturally. The presented exact discrete-time model of the SyRM can be applied for the design, analysis, and implementation of the controllers and observers. Based on the exact discrete-time model of the machine, the gains of a 2DOF state-space controller were calculated. Digital implementation requires the need for including the computational time delay and delay due to the ZOH inside the controller. Both of these delays were included in the control algorithm.

The controller based on the exact discrete-time model of the SyRM was compared with the controllers based on the continuous-time design (emulation) and the series expansion of the exact discrete-time model of the machine. The series expansions with one and two terms of the Taylor series expansion were used. In these controllers (emulation and series expansions), the ZOH of the stator input voltage was assumed in rotor coordinates. The computational requirements of the model increases with the increase in the number of terms of the Taylor series expansion. The emulation-based design gives poor performance in comparison with other controllers. The other benchmark methods, such as series expansions give better performance than the emulation-based design, with the two term expansion very close to the exact model in terms of performance. As the fundamental frequency increases, the oscillations were increased and the performance deteriorates for the benchmark methods.

The performance of the controller based on the exact discrete-time model of the SyRM was better than all the other benchmark controllers studied. The robustness of these methods against parameter errors was analyzed. The stability maps show that the exact discrete-time design has a comparatively larger stable region (against

inductance errors) than the other controllers. The results also show that the robustness of the current controllers is insensitive to the errors in the stator resistance. The current controllers were investigated using the simulations. The simulation results agree reasonably with the stability analysis. The emulation-based design had the poorest performance and the results from the series expansion with two terms were comparable to the exact model. The experiments were performed on a 6.7-kW SyRM drive. The experimental results were in accordance with the simulations and stability analysis. One factor which reduces the performance of the controllers is the magnetic saturation. In experiments, the saturation model was included in the controllers, but it still needs some improvements to properly incorporate the incremental or differential inductance.

A suitable topic for future research is to improve the existing saturation model by including the effect of the incremental inductance. Next stage would be to design a sensor-less control by implementing a suitable discrete-time rotor-position observer. A torque maximizing and loss-minimizing controllers will be developed for high speed applications.

Bibliography

[1] P. C. Krause, O. Wasynczuk, and S. D. Sudhoff, *Analysis of Electric Machinery and Drive Systems.* Piscataway, NJ: IEEE Press, 2002.

[2] A. Boglietti and M. Pastorelli, "Induction and synchronous reluctance motors comparison," Orlando, FL, Nov. 2008, pp. 2041–2044.

[3] B. Zaghdoud and A. Saadoun, "Inductances calculation of permanent magnet synchronous machine," *Int. Journ. of Comp. & Elec. Eng.*, vol. 6, no. 3, Jun. 2014.

[4] P. WaIde, C. U. Brunner *et al.*, "Energy-efficiency policy opportunities for electric motor-driven systems," OECD Publishing, Tech. Rep., 2011.

[5] M. Hinkkanen, Z. Qu, H. A. A. Awan, T. Tuovinen, and F. Briz, "Current control for IPMSM drives: direct discrete-time pole-placement design," in *Proc. IEEE WEMDCD'2015*, Torino, Italy, Mar. 2015, submitted.

[6] T. M. Rowan and R. J. Kerkman, "A new synchronous current regulator and an analysis of current-regulated PWM inverters," *IEEE Trans. Ind. Appl.*, vol. IA-22, no. 4, pp. 678–690, July/Aug. 1986.

[7] L. Harnefors and H.-P. Nee, "Model-based current control of AC machines using the internal model control method," *IEEE Trans. Ind. Appl.*, vol. 34, no. 1, pp. 133–141, Jan./Feb. 1998.

[8] F. Briz del Blanco, M. W. Degner, and R. D. Lorenz, "Dynamic analysis of current regulators for AC motors using complex vectors," *IEEE Trans. Ind. Appl.*, vol. 35, no. 6, pp. 1424–1432, Nov./Dec. 1999.

[9] F. Briz, M. W. Degner, and R. D. Lorenz, "Analysis and design of current regulators using complex vectors," *IEEE Trans. Ind. Appl.*, vol. 36, no. 3, pp. 817–825, May/June 2000.

[10] H. Kim and R. D. Lorenz, "Improved current regulators for IPM machine drives using on-line parameter estimation," in *Conf. Rec. IEEE-IAS Annu. Meeting*, vol. 1, Pittsburgh, PA, Oct. 2002, pp. 86–91.

[11] K.-K. Huh and R. D. Lorenz, "Discrete-time domain modeling and design for AC machine current regulation," in *Conf. Rec. IEEE-IAS Annu. Meeting*, New Orleans, LA, Sept. 2007, pp. 2066–2073.

[12] W. Peters, T. Huber, and J. Böcker, "Control realization for an interior permanent magnet synchronous motor (IPMSM) in automotive drive trains," in *Conf. PCIM 2011*, vol. 1, Nuremberg, Germany, May 2011, pp. 98–103.

[13] W. Peters and J. Böcker, "Discrete-time design of adaptive current controller for interior permanent magnet synchronous motors (IPMSM) with high magnetic saturation," in *Proc. IEEE IECON'13*, Vienna, Austria, Nov. 2013, pp. 6608–6613.

[14] H. Kim, M. W. Degner, J. M. Guerrero, F. Briz, and R. D. Lorenz, "Discrete-time current regulator design for AC machine drives," *IEEE Trans. Ind. Appl.*, vol. 46, no. 4, pp. 1425–1435, July/Aug. 2010.

[15] M. Hinkkanen, "Flux estimators for speed-sensorless induction motor drives," Ph.D. dissertation, Dept. Elect. Commun. Eng., Helsinki Univ. Tech., Espoo, Finland, Sept. 2004.

[16] A. Piippo, "An adaptive observer with signal injection for interior permanent magnet synchronous motors," Ph.D. dissertation, Dept. Elect. Eng., Helsinki Univ. Tech., Espoo, Finland, May 2008.

[17] ABB Drives Group, "Direct torque control - the world's most advanced AC drive technology, Technical guide no. 1," 2011.

[18] J.-S. Yim, S.-K. Sul, B.-H. Bae, N. R. Patel, and S. Hiti, "Modified current control schemes for high-performance permanent-magnet AC drives with low sampling to operating frequency ratio," *IEEE Trans. Ind. Appl.*, vol. 45, no. 2, pp. 763–771, Mar./Apr. 2009.

[19] Y.-S. Jeong and S.-K. Sul, "Analysis and design of a decoupling current controller for ac machines: A unified transfer-matrix approach," in *Conf. Rec. IEEE-IAS Annu. Meeting*, vol. 1. IEEE, 2005, pp. 751–758.

[20] B.-H. Bae and S.-K. Sul, "A compensation method for time delay of full-digital synchronous frame current regulator of PWM AC drives," *IEEE Trans. Ind. Appl.*, vol. 39, no. 3, pp. 802–810, May/June 2003.

[21] L. Harnefors, *Control of Variable-Speed Drives*. Västerås, Sweden: Applied Signal Processing and Control, Department of Electronics, Mälardalen University, 2003.

[22] M. Hinkkanen, "S-81.3300 Control of Electric Drives, Lecture notes," Aalto University, School of Electrical Engineering, Espoo, Finland, 2014.

[23] G. F. Franklin, J. D. Powell, and M. Workman, *Digital Control of Dynamic Systems*, 3rd ed. Menlo Park, CA: Addison-Wesley, 1997.

[24] L. Harnefors, M. Hinkkanen, and O. Wallmark, *Control of Voltage-Source Converters and Variable-Speed Drives, Lecture notes*, Västerås, Sweden, 2014.

[25] N. S. Nise, *Control Systems Engineering, 6th Edition.* John Wiley & Sons, 2007.

[26] J. S. Lee, C.-H. Choi, J.-K. Seok, and R. D. Lorenz, "Deadbeat-direct torque and flux control of interior permanent magnet synchronous machines with discrete time stator current and stator flux linkage observer," *IEEE Trans. Ind. Appl.*, vol. 47, no. 4, pp. 1749–1758, July/Aug. 2011.

[27] T. Geyer, "Model predictive direct torque control: derivation and analysis of the state-feedback control law," *IEEE Trans. Ind. Appl.*, vol. 49, no. 5, pp. 2146–2157, Sept./Oct. 2013.

[28] F. Morel, X. Lin-Shi, J.-M. Retif, B. Allard, and C. Buttay, "A comparative study of predictive current control schemes for a permanent-magnet synchronous machine drive," *IEEE Trans. Ind. Electron.*, vol. 56, no. 7, pp. 2715–2728, 2009.

[29] H.-T. Moon, H.-S. Kim, and M.-J. Youn, "A discrete-time predictive current control for PMSM," *IEEE Trans. Power Electron.*, vol. 18, no. 1, pp. 464–472, 2003.

[30] K.-H. Kim and M.-J. Youn, "A simple and robust digital current control technique of a PM synchronous motor using time delay control approach," *IEEE Trans. Power Electron.*, vol. 16, no. 1, pp. 72–82, 2001.

[31] A. Altomare, A. Guagnano, F. Cupertino, and D. Naso, "Discrete-time control of high speed salient machines," in *Proc. IEEE ECCE'14*, Sept. 2014, pp. 3528–3534.

[32] L. Harnefors, K. Pietiläinen, and L. Gertmar, "Torque-maximizing field-weakening control: design, analysis, and parameter selection," *IEEE Trans. Ind. Electron.*, vol. 48, no. 1, pp. 161–168, Feb. 2001.

[33] O. Wallmark, S. Lundberg, and M. Bongiorno, "Input admittance expressions for field-oriented controlled salient PMSM drives," *IEEE Trans. Power Electron.*, vol. 27, no. 3, pp. 1514–1520, Mar. 2012.

[34] R. Gessing, "Comments on "a modification and the Tustin approximation" with a concluding proposition," *IEEE Trans. Autom. Control*, vol. 40, no. 5, pp. 942–944, May 1995.

[35] T. Tuovinen, "Model-based position estimation for synchronous reluctance motor drives," Ph.D. dissertation, Dept. Elect. Eng. & Autom., Aalto Univ., Espoo, Finland, Aug. 2014.

[36] Z. Qu, T. Tuovinen, and M. Hinkkanen, "Inclusion of magnetic saturation in dynamic models of synchronous reluctance motors," in *Proc. ICEM'12*, Marseille, France, Sept. 2012, pp. 994–1000.

Appendix A

The elements of system matrix $\boldsymbol{A}_\mathrm{d}$ and input matrices $\boldsymbol{B}_\mathrm{d}$ and $\boldsymbol{b}_\mathrm{d}$ are as follows,

$$\boldsymbol{A}_\mathrm{d} = \mathrm{e}^{\boldsymbol{A}_\mathrm{c} T_\mathrm{s}} = \begin{bmatrix} a_{\mathrm{d}11} & a_{\mathrm{d}12} \\ a_{\mathrm{d}21} & a_{\mathrm{d}22} \end{bmatrix} \tag{A.1}$$

The closed-form solutions for the elements are given by

$$a_{\mathrm{d}11} = \mathrm{e}^{-\sigma T_\mathrm{s}} \left[\cosh(\underline{\gamma} T_\mathrm{s}) - \delta \frac{\sinh(\underline{\gamma} T_\mathrm{s})}{\underline{\gamma}} \right] \tag{A.2a}$$

$$a_{\mathrm{d}22} = \mathrm{e}^{-\sigma T_\mathrm{s}} \left[\cosh(\underline{\gamma} T_\mathrm{s}) + \delta \frac{\sinh(\underline{\gamma} T_\mathrm{s})}{\underline{\gamma}} \right] \tag{A.2b}$$

$$a_{\mathrm{d}21} = -a_{\mathrm{d}12} = -\omega_\mathrm{m} \mathrm{e}^{-\sigma T_\mathrm{s}} \frac{\sinh(\underline{\gamma} T_\mathrm{s})}{\underline{\gamma}} \tag{A.2c}$$

where[1]

$$\sigma = \frac{R_\mathrm{s}}{2} \left(\frac{1}{L_\mathrm{d}} + \frac{1}{L_\mathrm{q}} \right), \quad \delta = \frac{R_\mathrm{s}}{2} \left(\frac{1}{L_\mathrm{d}} - \frac{1}{L_\mathrm{q}} \right) \tag{A.3}$$
$$\underline{\gamma} = \sqrt{\delta^2 - \omega_\mathrm{m}^2}$$

The input matrix $\boldsymbol{B}_\mathrm{c}^\mathrm{s}(t)$ corresponding to the stator voltage is time variant. Hence, the discrete-time input matrix becomes

$$\boldsymbol{B}_\mathrm{d} = \int_0^{T_\mathrm{s}} \mathrm{e}^{\boldsymbol{A}_\mathrm{c} \tau} \boldsymbol{B}_\mathrm{c}^\mathrm{s}(T_\mathrm{s} - \tau) \mathrm{d}\tau \cdot \mathrm{e}^{\vartheta_\mathrm{m}(0) \boldsymbol{J}} = \begin{bmatrix} b_{\mathrm{d}11} & b_{\mathrm{d}12} \\ b_{\mathrm{d}21} & b_{\mathrm{d}22} \end{bmatrix} \tag{A.4}$$

[1] If $\omega_\mathrm{m}^2 > \delta^2$, then $\underline{\gamma} = \mathrm{j}\gamma_\mathrm{im} = \mathrm{j}\sqrt{\omega_\mathrm{m}^2 - \delta^2}$ is imaginary. All the matrix elements remain real since $\cosh(\mathrm{j}\gamma_\mathrm{im} T_\mathrm{s}) = \cos(\gamma_\mathrm{im} T_\mathrm{s})$ and $\sinh(\mathrm{j}\gamma_\mathrm{im} T_\mathrm{s})/(\mathrm{j}\gamma_\mathrm{im}) = \sin(\gamma_\mathrm{im} T_\mathrm{s})/\gamma_\mathrm{im}$ hold due to the properties of hyperbolic functions. Furthermore, for $\underline{\gamma} = 0$, these functions reduce to $\cosh(\underline{\gamma} T_\mathrm{s}) = \sinh(\underline{\gamma} T_\mathrm{s})/\underline{\gamma} = 1$.

The closed-form solutions for the matrix elements are[2]

$$\begin{aligned} b_{\mathrm{d}11} = K\Big[& g_1 \cos(\omega_{\mathrm{m}} T_{\mathrm{s}}) - 2(\sigma-\delta)\delta\omega_{\mathrm{m}} \sin(\omega_{\mathrm{m}} T_{\mathrm{s}}) \\ & - g_1 a_{\mathrm{d}11} + (\sigma+\delta)\omega_{\mathrm{m}}^2 (a_{\mathrm{d}11} - a_{\mathrm{d}22}) \Big] \end{aligned} \tag{A.5a}$$

$$\begin{aligned} b_{\mathrm{d}22} = K\Big[& g_2 \cos(\omega_{\mathrm{m}} T_{\mathrm{s}}) + 2(\sigma+\delta)\delta\omega_{\mathrm{m}} \sin(\omega_{\mathrm{m}} T_{\mathrm{s}}) \\ & - g_2 a_{\mathrm{d}22} + (\sigma-\delta)\omega_{\mathrm{m}}^2 (a_{\mathrm{d}22} - a_{\mathrm{d}11}) \Big] \end{aligned} \tag{A.5b}$$

$$\begin{aligned} b_{\mathrm{d}12} = K\Big[& 2(\sigma-\delta)\delta\omega_{\mathrm{m}} \cos(\omega_{\mathrm{m}} T_{\mathrm{s}}) + g_1 \sin(\omega_{\mathrm{m}} T_{\mathrm{s}}) \\ & - 2(\sigma-\delta)\delta\omega_{\mathrm{m}} a_{\mathrm{d}11} + g_2 a_{\mathrm{d}21} \Big] \end{aligned} \tag{A.5c}$$

$$\begin{aligned} b_{\mathrm{d}21} = K\Big[& 2(\sigma+\delta)\delta\omega_{\mathrm{m}} \cos(\omega_{\mathrm{m}} T_{\mathrm{s}}) - g_2 \sin(\omega_{\mathrm{m}} T_{\mathrm{s}}) \\ & - 2(\sigma+\delta)\delta\omega_{\mathrm{m}} a_{\mathrm{d}22} - g_1 a_{\mathrm{d}21} \Big] \end{aligned} \tag{A.5d}$$

where

$$K = \frac{1}{(\sigma^2-\delta^2)^2 + 4\sigma^2\omega_{\mathrm{m}}^2} \tag{A.6a}$$

$$g_1 = (\sigma-\delta)^2(\sigma+\delta) + 4\sigma\omega_{\mathrm{m}}^2 \tag{A.6b}$$

$$g_2 = (\sigma+\delta)^2(\sigma-\delta) + 4\sigma\omega_{\mathrm{m}}^2 \tag{A.6c}$$

The input matrix corresponding to the PM flux is

$$\boldsymbol{b}_{\mathrm{d}} = \int_0^{T_{\mathrm{s}}} \mathrm{e}^{\boldsymbol{A}_{\mathrm{c}}\tau} \mathrm{d}\tau \cdot \boldsymbol{b}_{\mathrm{c}} = \begin{bmatrix} b_{\mathrm{d}1} \\ b_{\mathrm{d}2} \end{bmatrix} \tag{A.7}$$

where the elements are given by

$$b_{\mathrm{d}1} = H\left[(\sigma-\delta)(1-a_{\mathrm{d}11}) - \omega_{\mathrm{m}} a_{\mathrm{d}21}\right] \tag{A.8a}$$

$$b_{\mathrm{d}2} = H\left[-\sigma a_{\mathrm{d}21} + \omega_{\mathrm{m}}\left(\frac{a_{\mathrm{d}11}+a_{\mathrm{d}22}}{2} - 1\right)\right] \tag{A.8b}$$

and

$$H = \frac{\sigma+\delta}{(\sigma+\delta)(\sigma-\delta)+\omega_{\mathrm{m}}^2} \tag{A.9}$$

[2]In the derivation, it is important to notice that $\mathrm{e}^{x+y} = \mathrm{e}^x\mathrm{e}^y$ does not hold for matrix exponentials in general.